Insights from Microstructure and Mechanical Property Comparisons of Three Pilgered Ferritic ODS Tubes

Caleb P. Massey, Philip D. Edmondson, Maxim N. Gussev, Keyou Mao, Tim Gräning, Thomas J. Nizolek, Stuart Maloy, Denis Sornin, Yann Decarlan, Sebastien N. Dryepondt, et al.

Insights from microstructure and mechanical property comparisons of three pilgered ferritic ODS tubes ☆

Caleb P. Massey [a,*], Philip D. Edmondson [a], Maxim N. Gussev [a], Keyou Mao [a], Tim Gräning [a], Thomas J. Nizolek [b], Stuart A. Maloy [b], Denis Sornin [c], Yann de Carlan [c], Sebastien N. Dryepondt [a], David T. Hoelzer [a]

[a] Oak Ridge National Laboratory, Oak Ridge, TN 37831, USA
[b] Los Alamos National Laboratory, Los Alamos, NM 87545, USA
[c] Université Paris-Saclay, CEA, Service de Recherches Métallurgiques Appliquées, F-91191 Gif-sur-Yvette, France

HIGHLIGHTS

- Pilger processing is a viable path towards manufacturing thin-walled ODS alloys for cladding applications.
- Oxide morphology variations illustrate their size-dependent resistance to dislocation-shear during processing.
- Specimen failure at room temperature is dominated by grain boundary decohesion even for recrystallized ODS ferritic tubes
- Differences in predictive accuracy of hardening models are revealed when applied to highly anisotropic ODS microstructures.

GRAPHICAL ABSTRACT
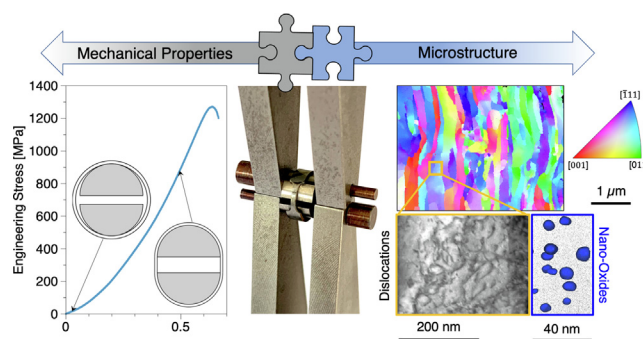
ARTICLE INFO

ABSTRACT

To develop advanced nuclear fuel claddings, two oxide dispersion strengthened (ODS) alloys were designed, manufactured, and evaluated. First, 12 %Cr alloy, is an ODS-version of ferritic steel, and second, 10 %Cr-6 %Al alloy, is a high-strength version of accident tolerant iron-chrome-aluminum alloy. Their properties and performance were compared with "classical" ODS material, 14 %Cr alloy 14WYT. Thin-walled (∼500 μm wall thickness) tubes were manufactured successfully using the pilgering technique. For all alloys, axial tensile specimens exhibited high tensile strength (>1 GPa) and reasonable plastic strains (10–17%). Ring tensile specimens, conversely, showed limited ductility (∼1%) with similar strengths to those measured in the axial orientation. The grain size, precipitate dispersion characteristics, and dislocation densities were then used to estimate yield strengths that were compared against room temperature axial and ring-pull tensile test data. The strengthening models showed mixed agreement with experimentally measured values due to the highly anisotropic microstructures of all three ODS tubes. These results illustrate the need for future model optimization to accommodate non-isotropic microstructures associated with components processed using rolling/pilgering approaches. In all cases,

atom probe tomography and energy-filtered transmission electron microscopy demonstrated that ODS structure survived multiple pilgering operations, and precipitate microstructure evolution matched well the state-of-the-art nanoprecipitate coarsening models.

1. Introduction

The primary obstacle preventing the development of large-scale, carbon-free nuclear fission and fusion energy systems centers around the lack of materials that can withstand the extreme conditions associated with hostile environments comprised of high-temperatures and irradiation doses [1,2]. Fortunately, one class of materials known as oxide dispersion strengthened (ODS) alloys has been extensively investigated for this purpose over the past several decades [3,4]. Because of a high number density of very stable oxide precipitates that interact with defects at the nanometer scale, ODS ferritic alloys boast high strength (>1 GPa) [5], creep resistance [5,6], and superb resistance to high-dose irradiation [7].

ODS alloys have historically been produced using a powder metallurgical route. Usually this involves mechanically alloying gas-atomized powders with dissolution of highly stable oxides to create a supersaturated solid solution of highly reactive elements and oxygen, followed by high-temperature consolidation to nucleate and grow a new homogeneous distribution of 2–4 nm stable oxide precipitates. Although a variety of consolidation methods have been explored for ODS alloy production, including hot extrusion, hot-isostatic pressing [8], and spark plasma sintering [9], the components generated have historically been rectangular bar or cylindrical rod geometries.

Although the geometry of critical components in practical applications deviates significantly from the initial geometries generated from conventional consolidation methodologies, a vast majority of the investigations of the thermal, mechanical, and irradiation stability of ODS alloys have occurred only on specimens with elementary geometries. This is partly attributed to the difficulty in processing such high-strength materials into complex geometries. For example, to translate a simple rod geometry to that of a thin-walled tube—one of the critical component geometries for the nuclear industry— the pilgering method has proven to be a viable, scalable processing method to date [4,10].

Recent international collaborations have successfully demonstrated the capability to produce thin-walled ODS alloys to > 1 m lengths. The collaboration between Oak Ridge National Laboratory (ORNL) and Nippon Nuclear Fuel Development Co. Ltd (NFD) resulted in two ODS alloys, ODS FeCrAl alloy CrAZY and ODS FeCr alloy OFRAC, being fabricated into 2 m long thin-walled (0.5 mm) tubes [10,11]. Additionally, a parallel collaboration between Los Alamos National Laboratory and the French Alternative Energies and Atomic Energy Commission (CEA) produced an ODS FeCr 14YWT thin-walled tube 1 m in length.

The purpose of this work is to ensure the tailored ODS structure survived multiple pilgering passes and the manufactured product (cladding tubes) inherited all benefits of the ODS material. To accomplish this task, a comprehensive suite of characterization methods was applied to all three aforementioned ODS alloys (OFRAC, CrAZY, and 14YWT). This analysis provides much needed characterization of post-pilger ODS tube microstructures to better translate existing state-of-the-art knowledge concerning strengthening and coarsening models into prototypic geometries needed for cladding applications.

2. Methodology

2.1. Materials

The three alloys investigated in this work are two new advanced ODS alloys (CrAZY and OFRAC) and one "classical" ODS material (14YWT). The compositions of each are provided in Table 1. Alloy 14YWT (Fe-14Cr-3 W-0.4Ti + 0.3Y$_2$O$_3$ in wt.%) was specifically designed to provide a combination of ultra-fine grains and high creep strength by maximizing the number density of nanoscale (Y,Ti,O)-rich precipitates throughout the microstructure. Initially developed at ORNL in 2000, 14YWT has an extensive mechanical properties database collected over the past 20 years [12].

More recently in 2018, the nanostructured ODS FeCr alloy OFRAC (Oak Ridge Fast Reactor Advanced Fuel Cladding) was designed with an impurity sequestration approach while utilizing best practices in the development efforts of alloys such as 14YWT, 12YWT, and MA957 [13]. The compositions are slightly different between OFRAC (Fe-12Cr-1Mo-0.3Ti-0.3Nb + 0.3Y$_2$O$_3$ in wt %) and 14YWT because of a slight drop in Cr (14–12 wt%) and a substitution of W with Mo for solid solution strengthening and high-temperature strength. However, the major difference is the addition of Nb for the sequestration of C and N in solution to produce a secondary distribution of MX-type fine carbonitrides throughout the microstructure.

The final alloy considered here is the ODS FeCrAl alloy CrAZY, with a composition of (Fe-10Cr-6Al-0.3Zr + 0.3Y$_2$O$_3$ in wt.%). CrAZY was designed for use in extreme environments that require enhanced oxidation resistance, in addition to high-temperature strength. Although CrAZY is also applicable to fusion applications because of its compatibility with Pb-Li coolants, the thin-walled tube produced in this work is designed for accident-tolerant fuel cladding applications in light water reactors. With its enhanced oxidation resistance in the presence of high-temperature steam, and with its beneficial high-temperature mechanical properties, ODS FeCrAl alloys have the potential to outperform wrought FeCrAl alloys and existing Zr-based alloys in accident scenarios [14].

Table 1
Measured chemical composition each alloy investigated in weight percent, measured by inductively coupled plasma–optical emission spectroscopy. Errors are either 2% relative to the mean or two significant digits in the last reported digit, whichever is the least.

wt %	14YWT-NFA1	OFRAC-OR1	CrAZY-OR1
Fe	81.76	85.90	83.57
Cr	14.40	12.35	9.71
Al	–	–	6.03
W	3.10	–	–
Mo	–	0.95	–
Ti	0.39	0.20	–
Nb	–	0.30	–
Zr	–	–	0.27
Y	0.21	0.18	0.22
O	0.116	0.087	0.114
C	0.016	0.026	0.069
N	0.008	0.011	0.017

Although the compositions vary from alloy to alloy, all three are fully ferritic and were produced using identical powder metallurgical processing steps at ORNL. These steps are presented in Fig. 1. First, identical mechanical alloying routines were applied for 40 h at rotational speeds varying from 350 to 600 rpm using a Zoz Simoloyer CM08 milling unit. For CrAZY and OFRAC, the gas-atomized ferritic powder was milled with yttria additions to achieve a homogeneous distribution of Y and O throughout the milled powder. For 14YWT, the gas-atomized ferritic powder already contained Y, so FeO was added instead to achieve a similar O content. Following mechanical alloying, all three types of powder were encapsulated in extrusion cans, degassed for 24 h at either 300 °C or 400 °C, and extruded using identical dies and area reduction ratios to form cylindrical rods of fully consolidated material. Following extrusion, the extruded rods were subjected to various stress-relief annealing treatments.

The extrusion temperatures and post-extrusion annealing temperatures varied between the three alloys. Both 14YWT and OFRAC were extruded at 850 °C, whereas CrAZY was extruded at a higher temperature of 1100 °C. The 14YWT alloy was annealed at 1200 °C for 3 h to ensure sufficient dislocation recovery, whereas OFRAC

was annealed at 1150 °C for 8 h. The longer anneal for the OFRAC alloy was necessary to reduce the microhardness of the material to a sufficient threshold (350 HV) to permit subsequent processing. Similarly, the CrAZY alloy was annealed for 5 h for the same reason, although the temperature was capped at 1000 °C to prevent excessive coarsening of the (Y,Al,O)-rich precipitates during the anneal.

All three alloys were then gun-drilled and subjected to a four-stage pilger/annealing process. Reduction ratios were the same for all alloys. Pilger-processing was performed at CEA using the high precision tube rolling technique for 14YWT, while pilgering was contracted through NFD for OFRAC and CrAZY. The major differences between the processing of the 14YWT and OFRAC/CrAZY were the intermediate annealing temperatures used for recovery/recrystallization of the microstructure between pilger steps. These differences and their consequential effects on the final microstructures are discussed in detail below.

Summarizing, for the first time, cladding tubes of sufficient length were manufactured from high-strength, modern ODS alloys. The final tubes of OFRAC and CrAZY measured 1.8 m in length with outer diameters (ODs) of 8.5 mm and wall thicknesses of 0.5 mm. In comparison, the 14YWT tube measured 1 m in length and mea-
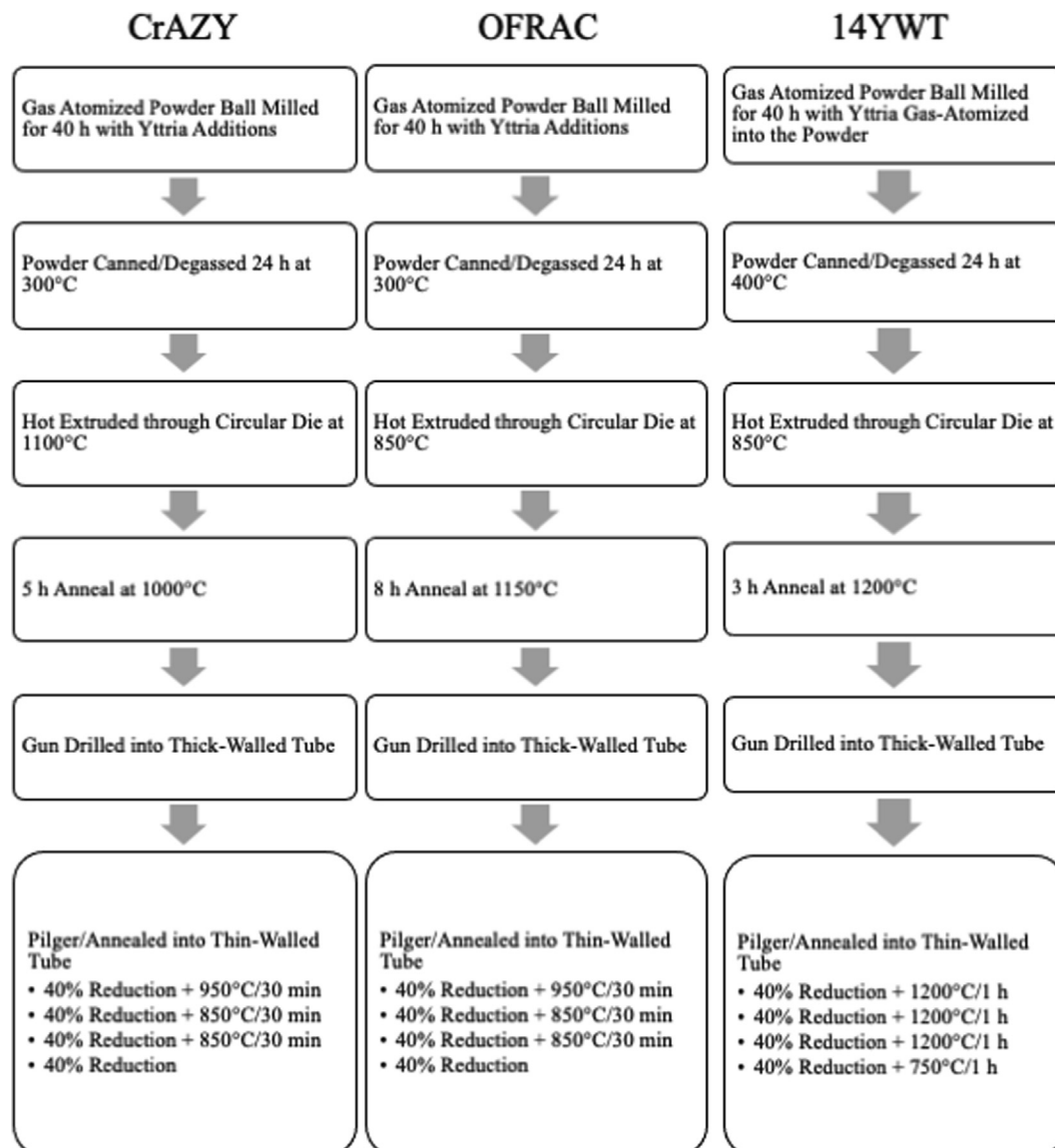

Fig. 1. Process diagrams for thin-walled ODS FeCr(Al) tubes produced via pilgering.

sured 10.7 mm in OD with a 0.48 mm wall thickness. Although the 14YWT tube was given a 750 °C stress-relief heat treatment, the OFRAC and CrAZY alloys are analyzed here in their as-pilgered condition. To allow for consistency in sample identification and comparison with other alloys in the literature, the heat designations for each alloy are as follows: 14YWT-NFA1, OFRAC-OR1, CrAZY-OR1.

2.2. Mechanical testing

Mechanical testing consisted of axial tensile and ring-pull tests on each tube using the specimen dimensions and fixtures shown in Fig. 2. The axial tensile specimen is a dual-gauge design with a gauge length of 4 mm and a width of 2 mm. The shoulder loaded nature of the axial tensile specimen allowed for simpler analysis of the load–displacement tensile curves, although, in some cases, slight differences in the yielding behavior of the multiple gauge sections caused some increased uncertainty because of the smearing of points on the engineering tensile curve, such as the onset of yielding. The ring-pull specimen is a single-gauge design with a width of 3 mm and a linear gauge length of 3 mm. The test frame consists of two D-shaped mandrels connected to the fixture by support pins. For the smaller 7.5 mm inner diameter (ID) tubes of OFRAC and CrAZY, mandrels with an OD of 7 mm were used. The larger 14YWT tube (9.7 mm ID) required the use of larger mandrels with ODs of 8.5 mm. Teflon tape was used as a lubricant between the mandrels and the ring.

When a load is applied, the ring specimen deforms around the mandrels until the gap closes completely and the remainder of the test approximates a uniaxial tensile test. Of course, the bending stresses associated with the ring/mandrel gap closure makes the

translation from displacement to strain impractical without other methods such as digital image correlation. Consequently, for the purposes of this analysis, the load/displacement curve for ring-pull tests will only be converted to a stress/displacement curve.

An MTS hydraulic tensile machine was used to test specimens in air at room temperature using a strain rate of 10^{-3} s^{-1}. For ring tensile specimens, this strain rate was computed based on the arc length of the gauge which varied as a function of tube diameter for a constant linear gauge length.

2.3. Microstructure characterization

2.3.1. Scanning electron microscopy and backscatter diffraction

As-received tubes were sectioned and metallographically polished with a final colloidal silica (0.05 μm) finish. Scanning electron microscope (SEM) images and electron backscatter diffraction (EBSD) data were collected using a TESCAN MIRA3 SEM equipped with an Oxford Symmetry EBSD detector. Fractography was performed using the same instrument at an accelerating voltage of 20 kV in secondary electron imaging mode.

All EBSD data were collected using a 30 kV accelerating voltage with a 4 nA beam current. To prevent anisotropic grain morphologies from affecting grain size statistics, imaging was conducted along the longitudinal orientation (i.e., the tube axis was oriented vertically in the EBSD scans). To optimize scan times and resolution, multiple different scan areas were analyzed for all three tubes. For major axis grain size determinations, EBSD scans were collected for OFRAC and CrAZY over areas of 50 μm × 200 μm (width × height) with a step size of 0.15 μm. For 14YWT, the scan area was 400 μm × 1000 μm and the step size was 1 μm. For minor axis grain size and texture determination, identical scans of areas 150 μm × 50 μm and step size of 0.075 μm were collected for all alloys. The sample tilt angle was 70°, while the working distance was 18 mm.

EBSD data was analyzed using EDAX OIM Analysis version 8.1. A grain tolerance angle of 5° was used for grain identification and quantification. Grains comprising an area less than 10 pixels were omitted from datasets to prevent erroneously identified grains from affecting grain size statistics. For visualization purposes, one iteration of grain confidence index correlation data cleanup was applied to each dataset.

Orientation calculations were performed using the generalized spherical harmonic series expansion approach with orthotropic sample symmetry. For the calculation, the series rank was 16 and the Gaussian halfwidth was 5°. Taylor and Schmid factors were exported for each point and each grain based on the orientation of the applied load (either parallel or perpendicular to the pilgering direction). Finally, the area-weighted Taylor factor was computed for each EBSD dataset and loading combination.

The effective diameter was calculated for each grain under the assumption that (1) grain morphology can be approximated using a spheroidal grain shape [15], and (2) that the effective grain diameter can be approximated by the average distance a dislocation travels along the most favorable slip systems. This second assumption is consistent with Taylor's compatibility criterion, whereby at least five different slip systems need to be simultaneously active in each grain to guarantee grain boundary contact as the material undergoes straining [16]. Thus, using the average minor and major axis grain diameters from the EBSD data, the 5 most prevalent slip systems active in the body centered cubic (BCC) lattice were imported into Python for each datapoint and the slip length was computed for each slip plane/slip direction combination. It therefore follows that the average effective diameter for each anisotropic grain is the average chord length of this slip vector across the elliptical cross section. For visualization purposes, an example of this calculation is shown in Fig. 3 for a spheroidal grain of aspect
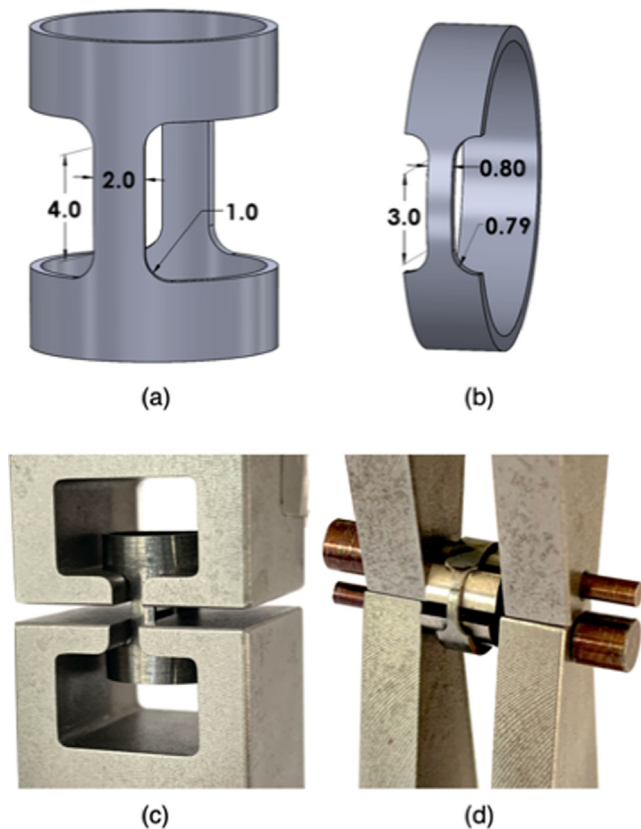

Fig. 2. Specimen types and dimensions used for (a) axial and (b) ring-pull tensile testing. The fixture used for axial tensile is shown in (c) and the fixture used for ring-pull tests is shown in (d). Dimensions in (a) and (b) are given in millimeters.
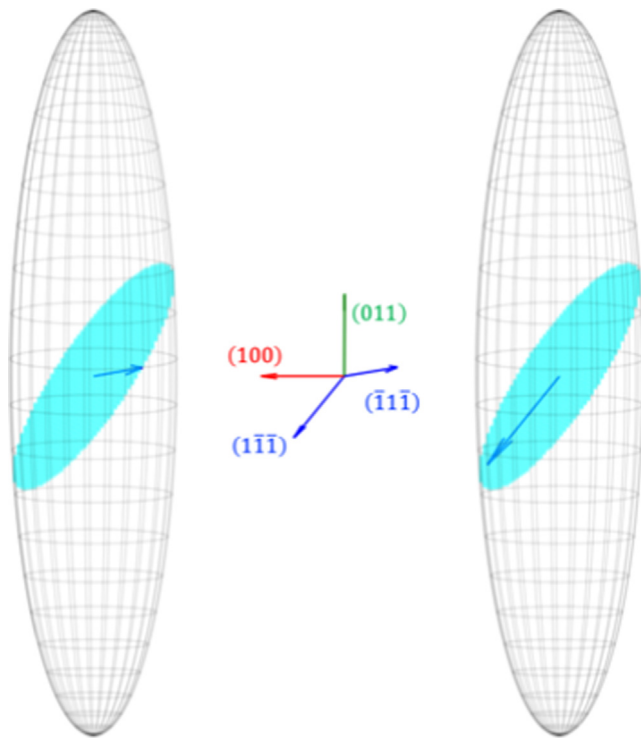
Fig. 3. Three-dimensional views of a spheroidal grain of aspect ratio 5:1 with major axis oriented parallel to [0 1 1] with resolved slip along $(110)\left[1\,\bar{1}\,\bar{1}\right]$ and $(110)\left[\bar{1}\,1\,\bar{1}\right]$.

ratio 5:1 and a major axis in the [0 1 1] direction resolved in example $(110)\left[1\,\bar{1}\,\bar{1}\right]$ and $(110)\left[\bar{1}\,1\,\bar{1}\right]$ directions.

2.3.2. Transmission electron microscopy

Transmission electron microscopy (TEM) specimens were prepared using focused ion beam (FIB) lift-out techniques [17]. A FEI Quanta 3D dual-beam FIB was used for all TEM lift outs. To ensure minimal Ga ion implantation in both the TEM lamella, decreasing accelerating voltages from 30 kV to 2 kV were used during the FIB thinning process. Final cleaning of the TEM lamella was performed using a Fischione Nanomill 1040 system with 900 eV Ar followed by plasma cleaning before TEM analysis.

Precipitate distributions were measured in each tube by the energy-filtered TEM (EFTEM) approach using a 200 kV JEOL JEM-2100F S/TEM. By filtering the Fe M-edge using an equipped Gatan imaging filter (GIF), Fe-M jump ratio maps were computed by dividing the Fe-M post edge (62 eV) image by the pre-edge (46 eV) image using 10 eV slit widths. In the resulting jump ratio map, regions with less Fe enrichment (i.e., oxygen-rich clusters in these alloys) appeared with dark contrast, which were then identified and quantified using the ImageJ software package [18].

The areal density of precipitates was converted to a volumetric density by computing the thickness of each lamella. The thickness was calculated by relating the attenuation of electrons through the lamella (the ratio of the unfiltered image to the zero loss image) to the inelastic scattering mean free path ($\sim$140 nm, depending on the collection angle of the TEM) [19]:

$$\frac{t}{\lambda} = \ln\left(\frac{unfiltered\ image}{zero-loss\ image}\right). \tag{1}$$

The same microscope was operated in scanning transmission electron microscope (STEM) mode for dislocation characterization. Dislocations were imaged on $\langle 1\,1\,1\rangle$ zone using the bright-field (BF)

STEM method [20]. The statistical analysis of the dislocation lines was performed using segmentation methods with Python and ImageJ. Individual TEM micrographs of dislocations were segmented by a 5×5 grid and filtered by a self-written background filtering Python code. Each remaining dislocation line was identified in ImageJ and measured to provide the length of each dislocation line ($l_i \sim$ 5–25 nm). At least 7 images with at least 300 dislocation lines were counted at different locations in each specimen for improved statistical confidence and accuracy. The dislocation density (ρ_D [m^{-2}]) was then calculated by the total length of dislocation lines ($\sum_N l_i$) divided by the measured volume ($A \cdot t$) using the equation:

$$\rho_D = \frac{\sum_N l_i}{A \cdot t}. \tag{2}$$

2.3.3. Atom probe tomography

APT was performed on each tube to further quantify nanoscale precipitation within each alloy and to directly compare with EFTEM methods. APT specimens were prepared using either an FEI Versa 3D dual-beam FIB-SEM or an FEI Helios 600 with final tip sharpening performed at 5 kV. Three of the APT datasets used in this work, specifically for the OFRAC alloy, were analyzed on a CAMECA LEAP 5000 XR instrument at the Max-Planck-Institut für Eisenforschung (MPIE) in Düsseldorf, Germany. These data were presented in detail in an earlier publication discussing precipitate/dislocation interactions [21]. The remaining three datasets for OFRAC, and the six datasets each for the CrAZY and 14YWT alloys, were analyzed on a CAMECA LEAP 4000X HR instrument at the Center for Nanophase Materials Sciences facility at ORNL. The sum of these APT runs provides a robust set of data to compare the dispersions measured using the EFTEM technique.

On both instruments, APT data were collected in laser pulsing mode using a laser energy of 32 pJ and a pulse frequency of 200 kHz. The target detection rate was set to 0.5%, and the specimen temperatures were held constant at 50 K during acquisition. APT data analysis was performed using the Integrated Visualization & Analysis Software (IVAS) package version 3.6.8 with the data reconstructed using a reverse point-projection method. Nanoscale precipitation was identified using a combination of the maximum separation method and the isosurface method [22–25]. For this analysis, the precipitate radius is reported as the Guinier radius [26], and the number density is computed using the method of Bachhav et al. [27]:

$$N_p = \frac{n_p \rho}{(N_{tot}/Q)}, \tag{3}$$

where n_p is the number of precipitates in the APT volume, ρ is the atomic density of α-Fe (84.3 atoms/nm^3), N_{tot} is the total number of ions detected in the control volume, and Q is the detection efficiency of the detector used (36% for 4000X HR and 52% for 5000 XR).

2.3.4. X-ray diffraction

To compare with STEM results, x-ray diffraction (XRD) was performed to estimate the dislocation densities of all three tubes. All materials have a BCC structure and were tested along the tube axis in Bragg-Brentano geometry.

For the XRD analysis, the modified Williamson-Hall equation was used [28]:

$$\Delta K \cong \frac{0.9}{D} + \left(\frac{\pi M^2 b^2}{2}\right)^{\frac{1}{2}} \rho^{\frac{1}{2}} K C^{\frac{1}{2}} + O\left(K^2 C\right), \tag{4}$$

which is the following in quadratic form [29]:

$$(\Delta K)^2 \cong \left(\frac{0.9}{D}\right)^2 + \left(\frac{\pi M^2 b^2}{2}\right) \rho K^2 C + O\left(K^4 C^2\right), \tag{5}$$

where D is the average crystallite size, $M = 2$ is a constant depending on the cut-off radius of dislocations, $K = 2\sin\theta/\lambda$, ΔK is the full width at half maximum (FWHM), b is the burgers vector of ferrite (0.248 nm), ρ is the average dislocation density, C is the average contrast factor of dislocations, and O indicates non-interpreted high-order terms. The average contrast factor in cubic crystals can be written as [30]:

$$C = C_{h00}\left(1 - qH^2\right), \tag{6}$$

with C_{h00} as the average contrast factor corresponding to the $h00$ type reflection and q as a constant depending on the elastic constants of the crystal. Assuming a ratio of 1:1 for screw and edge dislocations in all tested materials, a value of 0.19 was used for C_{h00} [30]. H was calculated for each peak using the equation:

$$H = \frac{h^2k^2 + h^2l^2 + k^2l^2}{h^2 + k^2 + l^2}. \tag{7}$$

The measurements were performed with adjustable slits of 0.5 mm to minimize beam spread on the surface of the tubes. This arrangement keeps the beam width to 0.5 mm at all angles of 2-Theta using the Bragg-Brentano geometry [31]. All measurements were taken using Cu-K$_\alpha$ radiation (λ = 1.540598 Å). The raw XRD data were instrument-corrected using the standardized LaB6 powder data and analyzed using TOPAS V6 software by Bruker. Additionally, a peak deconvolution without a Rachinger correction using Origin Pro software was performed. A pseudo Voigt peak fit (PsdVoigt1) was used to distinguish the $K_{\alpha 1}$ and $K_{\alpha 2}$ peaks, assuming a ratio of 2:1. A peak deconvolution for each single peak was conducted, sharing the FWHM and the profile shape factor for both resulting peaks. The center of each peak, which was determined using TOPAS software, was set and not allowed to change, whereas area, offset, FWHM, and the shape factor were variables that could be changed to reach a fit tolerance of 1×10^{-15}. The value q was calculated using a linear regression model in a python script for each material. The linear slope of each material for typical plot of ΔK against $KC^{1/2}$ was determined and used to calculate the dislocation density of each material using Eq. (4).

3. Results

3.1. Post-pilger microstructure of advanced claddings

The microstructures of each tube are shown using EBSD inverse pole figure (IPF) maps in Fig. 4. In all alloys, the grains have a highly anisotropic morphology, which is more extreme for the OFRAC and CrAZY alloys. The 14YWT tube grains are much larger and have significant amounts of intragranular orientation changes indicative of significant dislocation densities within the grains. This is based upon the observation that changes in lattice rotation within a grain can be equated to the density of geometrically necessary dislocations necessary to accommodate the orientation change. Regardless of alloy, all grains have a bamboo-like morphology elongated in the tube axis (vertical) direction of the EBSD images. The average major and minor axes for 14YWT grains are 74 and 6.5 μm, respectively, which equates to an aspect ratio of ~11. This is similar to aspect ratio measurements made for fully recrystallized ferritic ODS alloys elsewhere in the literature processed using similar methods [32,33]. In comparison, the OFRAC and CrAZY grains have major axes averaging 7 μm/13 μm and minor axes averaging 0.15 μm/0.16 μm.

It is well known that increased deformation leads to a larger driving force (and thus a lower threshold temperature) for recrystallization to occur. Although ODS ferritic alloys as a general rule are known for having high thermal stability, significant amounts of deformation promotes recrystallization at lower temperatures,

as has been routinely demonstrated for 14YWT, MA956, MA957, and others in the literature [34,35]. For the OFRAC and CrAZY tubes, the intermediate heat treatments were chosen to prevent recrystallization [11]. For the 14YWT alloy, the intermediate annealing temperature between pilger steps was 1200 °C, which caused full recrystallization between one of the pilgering steps. Although it is unclear at which intermediate annealing step this recrystallization and significant grain growth occurred, the significant deformation within the grains suggests that recrystallization or recovery could have occurred earlier in the pilger/annealing process. In this way, the dislocation-free recrystallized grains were then deformed at a later pilgering stage, resulting in the significant intragranular deformation noted in the final pilgered 14YWT structure.

When BCC alloys are deformed, the preferential slip of dislocations along preferred slip systems causes characteristic grain orientations to develop within the microstructure [36]. This preferred orientation (texture) has been extensively studied for ODS alloys because large textures can lead to orientation-specific mechanical properties [34,35,37–40]. Texture is usually visualized using orientation distribution function (ODF) plots that show a 2D representation of the density of various grain orientations in 3D space. This requires the simplification of observing all 3D orientation space (using Euler angles ϕ_1, Φ, and ϕ_2 for this purpose) to viewing only slices of one of the three Euler angles. Conveniently for BCC materials, all major texture components can be visualized using plots at constant angles of $\phi_2 = 0$ and 45°.

ODF plots are provided for each tube in Fig. 5. Grains are usually oriented such that the $\langle 110 \rangle$ orientation is parallel to the rolling or extrusion direction. This is known as α-fiber texture. For extruded material, the alpha-fiber texture commonly extends down the entirety of the green line shown in Fig. 5, indicating a distribution of orientations normal to the extrusion direction. However, following the extensive deformation associated with the tube pilgering process, the texture intensifies along certain α-fiber components, namely the $\{001\}\langle 110 \rangle$ and $\{111\}\langle 110 \rangle$ orientations. Texture in which the $\langle 111 \rangle$ orientation is parallel to the normal direction ($\langle 111 \rangle \| ND$) is referred to as γ-fiber. In the current alloys, the γ-fiber is minimal except for the components associated with the α-fiber, such as $\{111\}\langle 110 \rangle$. Interestingly, the 14YWT tube exhibits slightly different textures in comparison to the OFRAC and CrAZY tubes. In Fig. 5(a), a weak texture component $\{011\}\langle 100 \rangle$ is noted at $\phi_1 = 0°$, $\Phi = 45°$. Fig. 5(b) also shows the same weak texture component that extends from $\{011\}\langle 100 \rangle$ to $\{111\}\langle 110 \rangle$. Cross referencing this plot with the IPF maps in Fig. 4 confirms that some of the grains have a Goss texture $\{011\}\langle 100 \rangle$, which is a specific recrystallization texture that has been observed in ODS ferritic alloys following severe cold work [41]. Thus, the transition from $\{011\}\langle 100 \rangle$ to $\{111\}\langle 110 \rangle$ could indicate that the Goss grains were introduced during one of the earlier annealing treatments on the 14YWT alloy, and subsequent pilger-deformation is driving the texture back to $\{111\}\langle 110 \rangle$.

3.2. Dislocation and precipitate dispersion characteristics

Multiple methods were used to investigate the density of dislocations within the as-received tube microstructures. The first of these methods was the STEM approach, in which multiple BF electron micrographs were analyzed to directly count the number of dislocations in each control volume. This is the most direct method for dislocation density estimations, but it suffers from uncertainties in (1) identifying what features are to be counted, (2) the number of counted dislocations based on the $g * b$ invisibility criteria for diffraction contrast dislocation imaging, (3) errors in thickness measurements for the foil, and (4) field-of-view limitations.
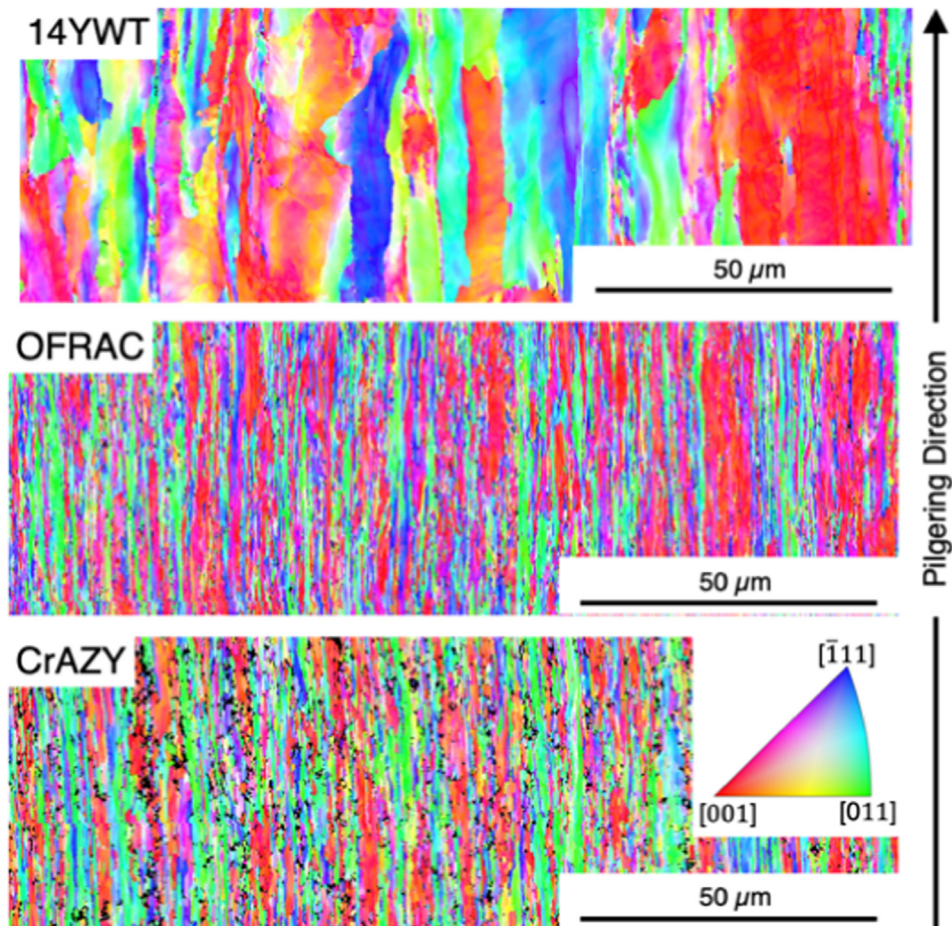
Fig. 4. EBSD IPF maps showing differences in grain size, morphology, and orientation. The tube axis (pilgering direction) is oriented vertically in all images.

With advances in automated contrast-based algorithms, issues associated with counting have been greatly minimized. Furthermore, imaging along ⟨111⟩-zone axis has been shown to greatly reduce the number of invisible dislocations using STEM methods [42]. This is partially because of the limiting of dislocation types fulfilling the $g * b$ invisibility criterion to the a/2⟨111⟩ edge and screw dislocation as well as the averaging of signal intensities over a wider range of incident illumination angles. Although errors in thickness measurements using the EFTEM approach can be appreciable (±20%) based on uncertainties in the calculation of λ [43], the larger error usually comes from the final issue of field-of-view limitations. Spatially dependent dislocation densities within alloys requires multiple averaged datasets for reliable statistics.

Fig. 6 shows typical dislocation networks seen in the tubes as imaged along the ⟨111⟩-zone axis. From an averaging of multiple images per specimen spanning different grains within each TEM lamella, the average dislocation densities were calculated to be $(3.96 ± 1.84) \times 10^{13}$ for 14YWT, $(2.16 ± 1.07) \times 10^{14}$ for OFRAC, and $(2.11 ± 1.41) \times 10^{14}$ m^{-2} for CrAZY.

Characteristic XRD profiles for each tube are illustrated with labeled peaks in Fig. 7. Using the measured peak widths, the corresponding ΔK against $KC^{1/2}$ plot in Fig. 8 was used to compute equivalent dislocation density. The dislocation densities estimated using the XRD method are provided in Table 2. These values are one to two orders of magnitude higher than those measured by STEM methods. One of the reasons for this is that the dislocation density estimated using the XRD method, although considering crystallite size and instrumental effects, mainly attributes broadening of the diffraction peak to a total equivalent dislocation den-

sity. Consequently, it does not omit the interaction of dislocation networks to form a new lower angle (5°–15°) lamellar grain boundaries. In fact, many of the dislocations that are generated during cold rolling reorient as geometrically necessary dislocations that separate regions deforming by different slip systems [44]. In comparison, the measured dislocation densities from the STEM images were mainly computed for dislocation networks within grains. From the high number of lamellar boundaries noted in the Fig. 4 EBSD maps, it is unsurprising that the XRD values are thus considerably higher. The other factor that could explain the larger discrepancy is that when using ions to thin TEM specimens, significant losses in dislocations (∼40%) have been shown to occur due to dislocation slip induced by stresses associated with sample preparation [45]. Important repercussions for this difference in dislocation density are discussed later in Section 4.1.

Precipitate dispersion and morphologies for all three tubes are illustrated for APT in Fig. 9 and for EFTEM in Fig. 10. For the 14YWT and OFRAC alloys, the nanoscale precipitates were enriched primarily in Y, Ti, and O. For CrAZY, the precipitates were enriched in Y, Al, and O. In this work, isoconcentration surfaces are used to show enclosed regions where the sum of the elements enriched in each precipitate exceed a given threshold. It was determined that the number of precipitates and their size were comparable to those identified using the maximum separation method when a concentration threshold of 1.5% (Y + Ti + O) was used for 14YWT/OFRAC or 1.5% (Y + Al + O) was used for CrAZY. Studies have investigated the nuances of APT artifacts (instrument resolution, trajectory aberrations, peak deconvolution, etc.), and how the compositions of nanoscale oxide precipitates can be corrected and
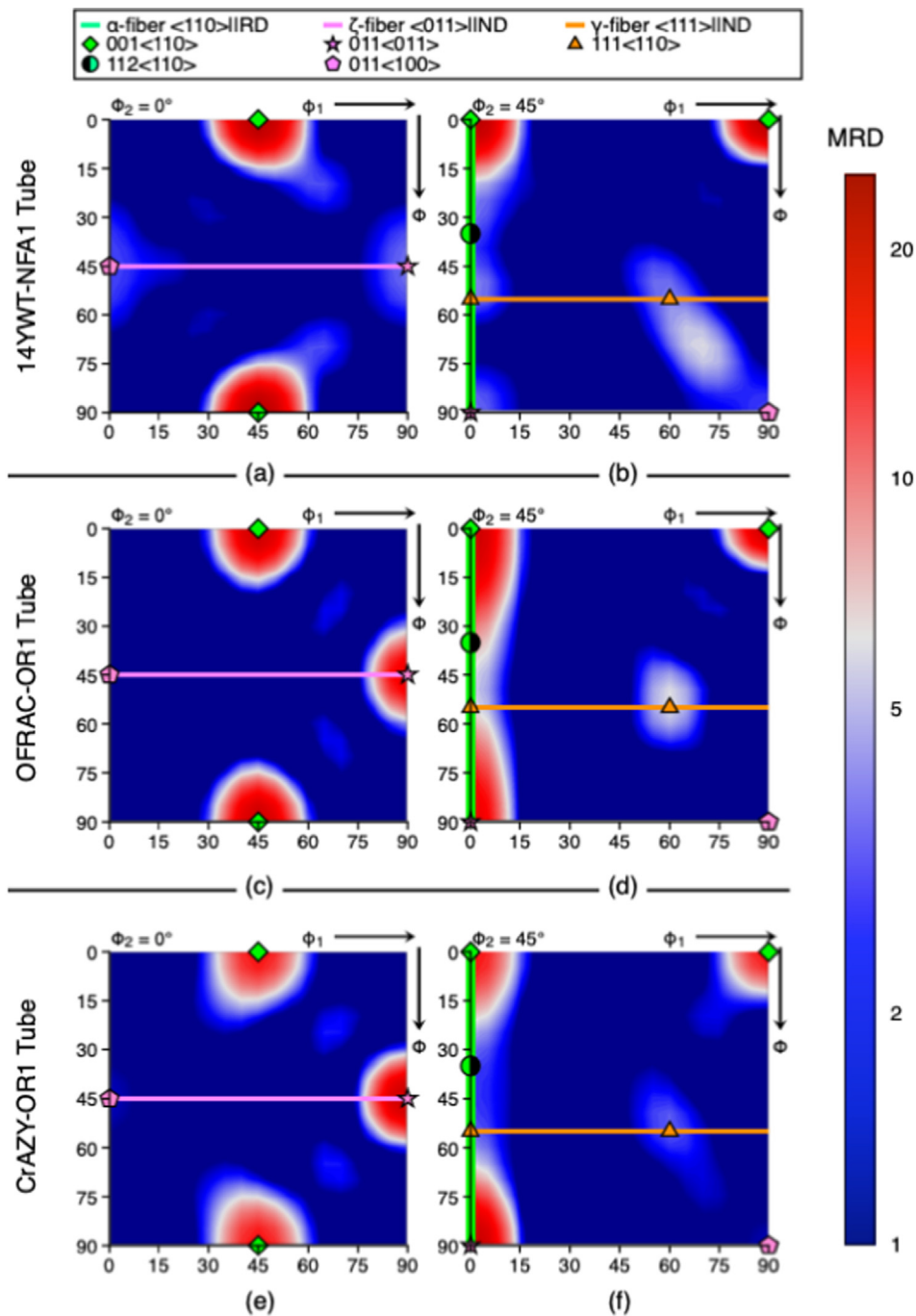
Fig. 5. ODF contour plots for each thin-walled tube computed from EBSD methods. All plots use Euler angle representation and highlight two characteristic slices at $\phi_2 = 0°$ and 45° where major rolling texture components for BCC materials are visible. All plots are normalized to the same color bar in units of multiples of random density.

identified [46,47]. For ODS FeCr alloys such as 14YWT and OFRAC, the most commonly observed oxide is $Y_2Ti_2O_7$, although constituent elements such as Y and O are routinely underestimated for (Y,Ti,O)-rich precipitates using the APT technique [6,13,48,49]. For ODS FeCrAl alloys with (Y,Al,O)-rich precipitates, such as the CrAZY alloy investigated here, the difficulty in deconvoluting the partitioning of Al contents of the particles with that of the surrounding FeCrAl matrix adds additional complexity to estimating precipitate compositions using APT. Even so, complementary techniques such as high-resolution STEM have confirmed the coexistence of multiple (Y,Al,O)-rich phases within the CrAZY alloy microstructure [50].

These APT (Fig. 9) and EFTEM (Fig. 10) images highlight different precipitate morphologies and distributions in each alloy. For the OFRAC alloy, many of the precipitates have an elongated ellipsoidal morphology, while others remain in a spheroidal shape. A detailed investigation into the elongated nature of the OFRAC tube precipitates can be found elsewhere [21], although it is important to note because similar trends may be noticeable in the CrAZY or 14YWT alloys, but to a lesser extent. It has been previously shown that plastic deformation can cause the dissolution of nano-oxides in an ODS matrix [51], but only with larger strain rates to those usually seen during tube pilgering. However, the differences in morphology here may suggest that smaller particles with lower
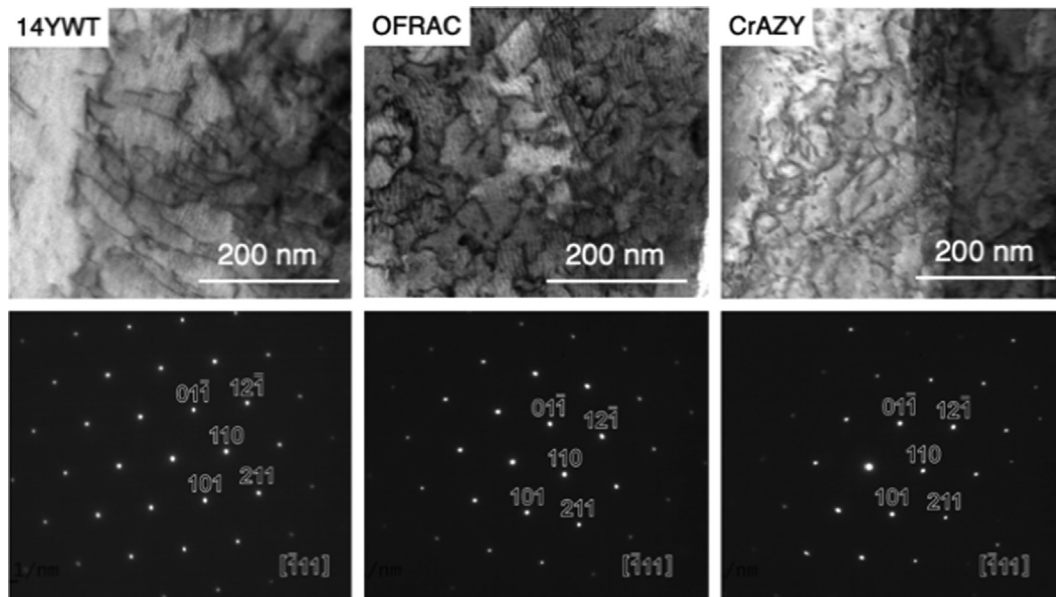
Fig. 6. Typical BF STEM images of dislocation networks in each ODS FeCr(Al) alloy tube. All micrographs are imaged along the ⟨111⟩-zone axis, as confirmed by the accompanying indexed diffraction patterns.
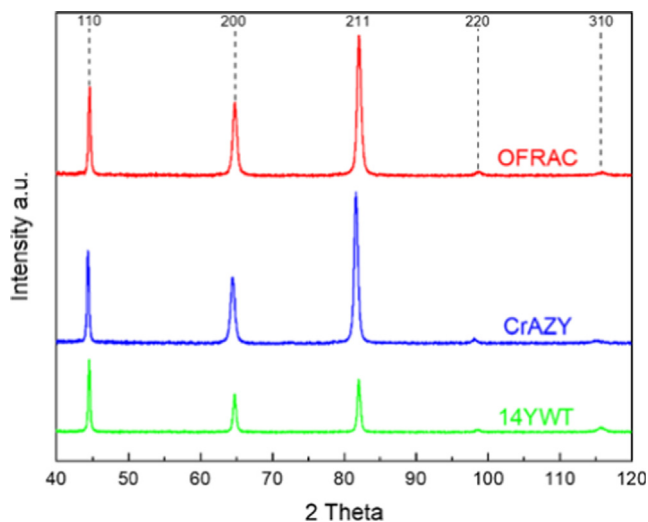

Fig. 7. Intensity XRD profiles in arbitrary units of the three materials are plotted against 2 Theta with a y-offset for comparison reasons. Corresponding hkl values for each peak are shown along the top of the figure.

Fig. 8. Linear slope fitting of the mod. Williamson-Hall plot for the three materials.

obstacle strength may be changing in shape due to localized dissolution and particle shear. The precipitates in the 14YWT and the CrAZY alloys are thus more spherical, but the number density of precipitates is lower in these two alloys. The EFTEM images show the preferential alignment of precipitates in all three alloys along the tube axis (indicated by white arrows in Fig. 10). This alignment of precipitates along preferential directions in directionally-deformed ODS alloys has been documented previously in the literature [34].

3.3. Post-pilgering mechanical behavior

The results of axial tensile and ring-pull tests are provided in Fig. 11. The OFRAC alloy exhibits the highest yield and ultimate tensile strength, while the 14YWT alloy measured the lowest. The average yield stresses for the axial specimens are as follows:
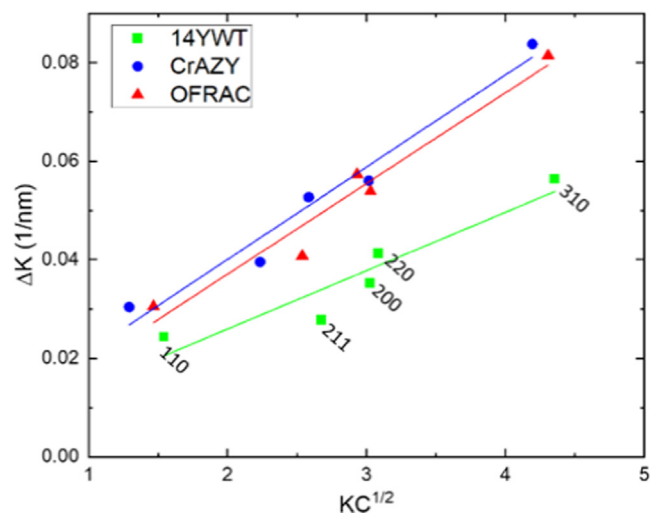
14YWT (887 ± 96 MPa), OFRAC (1201 ± 22 MPa), and CrAZY (1046 ± 33 MPa). The uniform elongation is also much larger for the axial 14YWT tensile tests than for the finer-grained ODS alloy variants. Interestingly, the total elongations at fracture were similar for all three alloys, regardless of the differences in grain structure. Additionally, for the two specimens tested in each condition, there was good repeatability in all tensile tests.

The differences in axial tensile response between the three alloys is directly attributable to the microstructure differences from thermomechanical processing. The larger-grained microstructure, coupled with the lower number density of precipitates owing to coarsening during the 1200 °C intermediate annealing treatments, resulted in lower strength for the 14YWT alloy. Conversely, the very fine grains of the OFRAC alloy provided more efficient Hall-Petch strengthening while the higher number density of dispersed particles further enhanced the strength through dislocation pinning. The axial tensile response of the CrAZY alloy lies somewhere between the OFRAC and 14YWT alloys. Its grain size

Table 2
Input and output data of the mod. Williamson-Hall analysis.

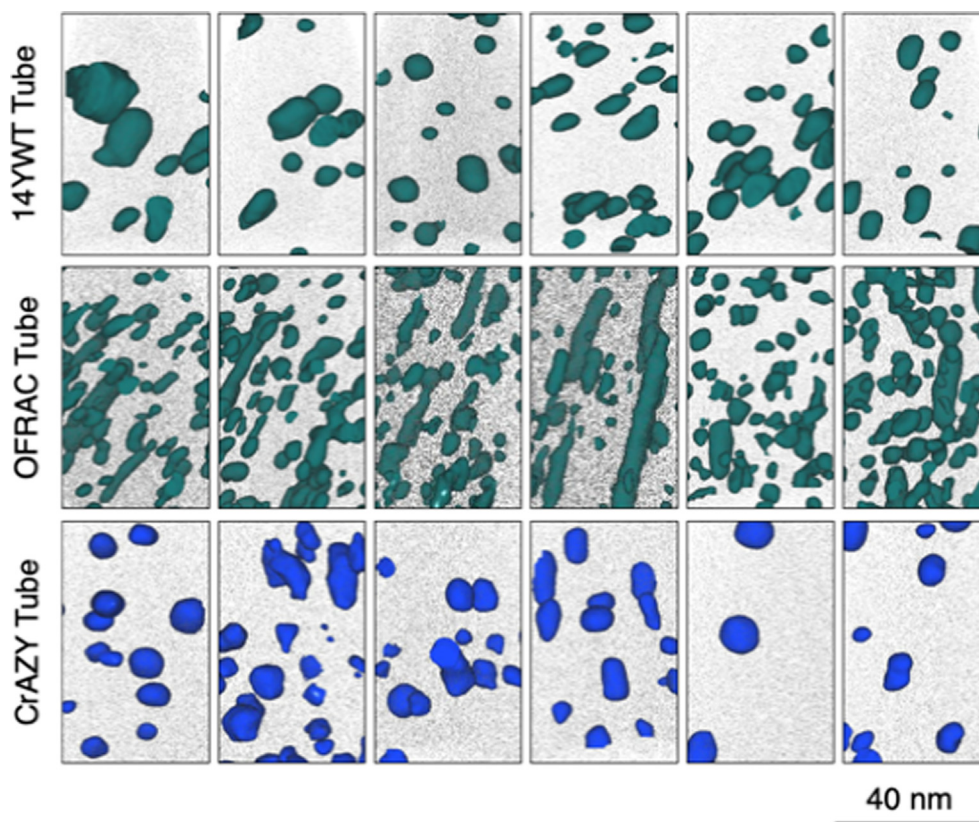| H^2	hkl	14YWT		CrAZY		OFRAC	
		2θ [°]	FWHM (ΔK)	2θ [°]	FWHM (ΔK)	2θ [°]	FWHM (ΔK)
0.25	110	44.48	0.252	44.32	0.309	44.53	0.311
0	200	64.69	0.404	64.42	0.620	64.74	0.599
0.25	211	81.93	0.360	81.56	0.496	82.00	0.512
0.25	220	98.41	0.596	98.01	0.747	98.56	0.814
0.09	310	115.58	0.987	115.03	1.430	115.70	1.404
q		1.924		2.537		2.131	
Dislocation Density (ρ) [m^{-2}]		3.64×10^{15}		9.09×10^{15}		8.77×10^{15}	

Fig. 9. APT volumes measuring $40 \times 40 \times 65$ nm^3 show the precipitate dispersions in each tube. Green isoconcentration surfaces highlight regions enriched in at least 1.5% (Y + Ti + O), and blue surfaces represent regions with 1.5% enrichment of (Y + Al + O). In each image, 0.1% of background Fe atoms are also presented as black dots. (For interpretation of the references to color in this figure legend, the reader is referred to the web version of this article.)

is very similar to that of OFRAC, but the particle dispersion is much coarser and lower in number density, which would qualitatively decrease the effectiveness of the dispersed particles as obstacles to dislocation motion.

The ring-pull response shows similar trends to the axial tensile response but requires some additional explanation. First, the OFRAC and CrAZY ring stress/displacement curves overlay well, whereas the 14YWT test requires significantly more displacement to reach a maximum stress level. This difference in response is a result of the difference in tube diameters and mandrels used for each test. The OFRAC and CrAZY alloys, with an ID of 7.5 mm, had a smaller gap between the 7 mm mandrel. Based on the initial gap, the displacement at which gap closure was estimated for these tubes was ~0.2 mm, which is consistent with the transition to a linear load/displacement portion of the ring tensile response in Fig. 11. For the 14YWT alloy with an ID of 9.7 mm, the largest available mandrel (8.5 mm) was used, which created a larger initial gap.

For this condition, the estimated displacement to close the gap was computed to be > 0.6 mm, which is consistent with the larger transition region where the ring specimen must deform around the mandrel to form the characteristic elliptical stadium shape reached during ring testing.

During a ring tensile test, it is possible that the bending of the ring specimen into the stadium shape causes local bending stresses and strains which locally yield portions of the ring specimen. Thus, the interpretation of the ring-pull load/displacement data is somewhat more complicated than a uniaxial tensile test. However, following the establishment of the characteristic stadium shape, a linear stress/strain region appears that is indicative of a quasi-elastic mechanical response before reaching a maximum tensile stress, ultimately resulting in necking and fracture. To simplify the ring-pull analysis in this work, it is therefore assumed that the 0.2% offset yield stress can be measured by standard engineering methods using the most linear portion of the stress/displace-
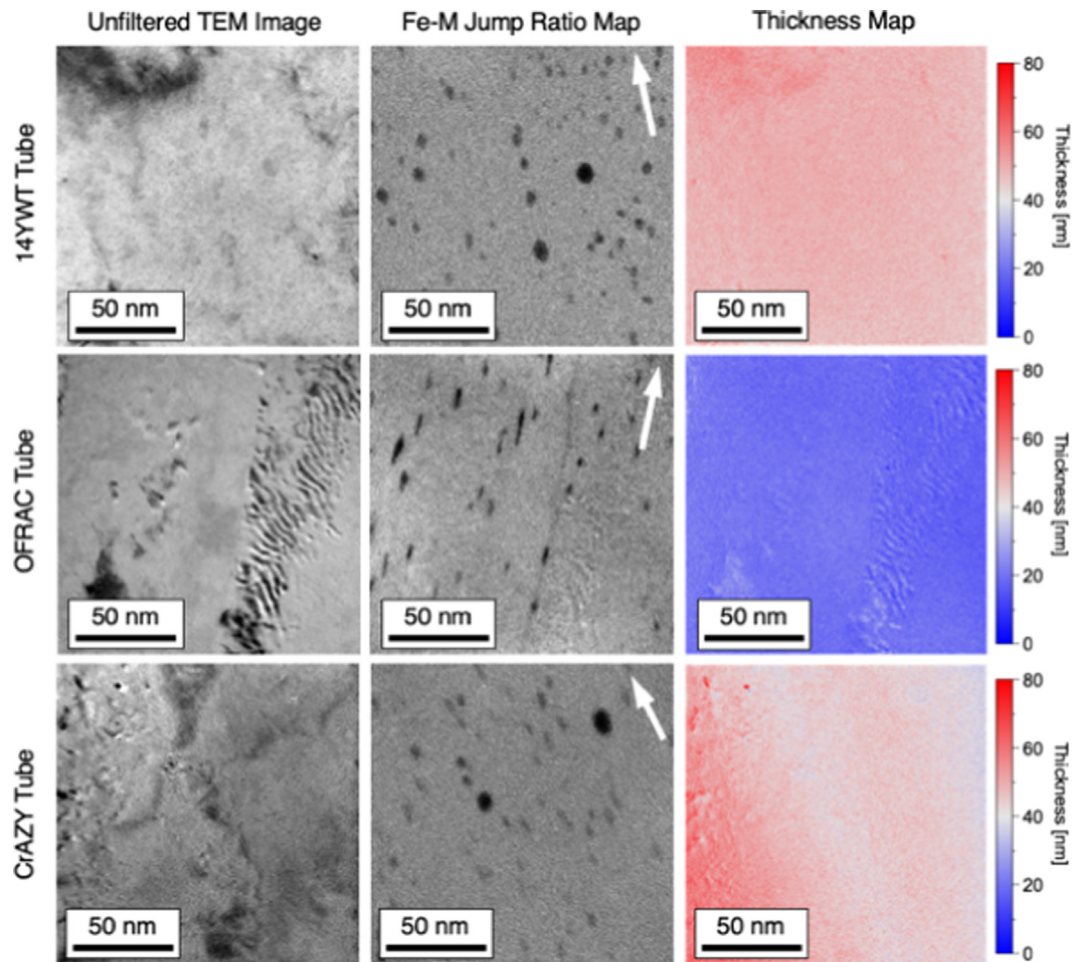
Fig. 10. Representative EFTEM maps for particle size and density calculations. The unfiltered TEM image of the region of interest is shown on the left, while the middle image is the jump ratio map for the Fe M-edge of the electron energy loss spectroscopy (EELS) spectrum. In the Fe-M jump ratio map, darker areas indicate a lack of Fe, while brighter regions indicate Fe enrichment. On the right, thickness maps and histograms are provided to convert precipitate areal density to number density.
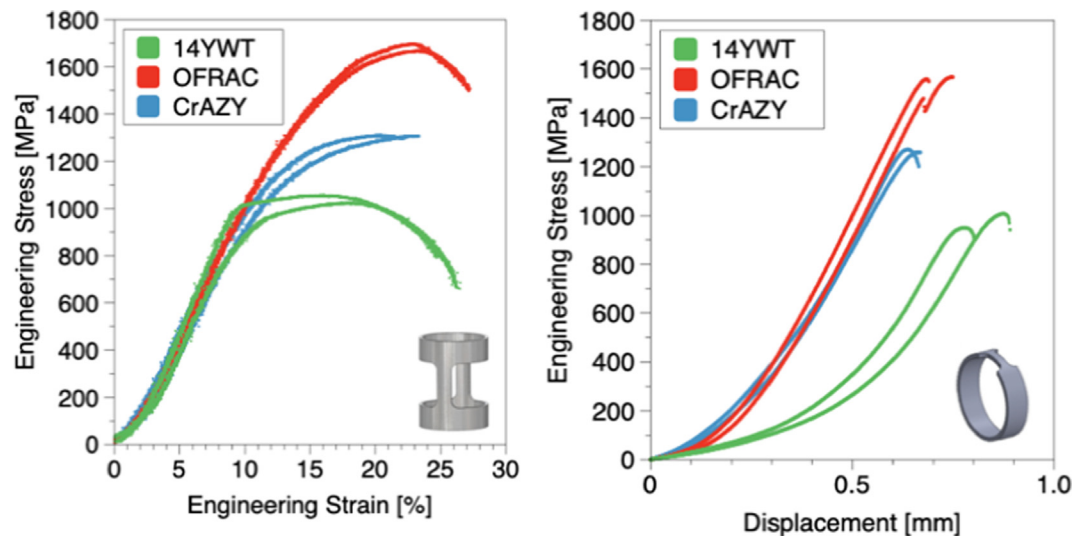
Fig. 11. Room temperature tensile response of axial (left) and ring-pull (right) specimens from each ODS tube. For axially loaded specimens, the engineering stress is plotted as a function of engineering strain, and for ring-pull specimens the stress is plotted as a function of crosshead displacement.

ment plot. The average estimated yield stresses for the ring specimens are as follows: 14YWT (960 ± 39 MPa), OFRAC (1495 ± 73 MPa), and CrAZY (1254 ± 20 MPa).

The ring-pull test specimens all exhibited minimal ductility before failure, which is in stark contrast to the axial tensile tube response. This contrast is attributed to the microstructural aniso-

Fig. 12. Fracture surface secondary electron images for axial tube specimens of (a) 14YWT and (b) OFRAC show similar failure modes for both alloys. Although ductile dimpling is apparent on both fracture surf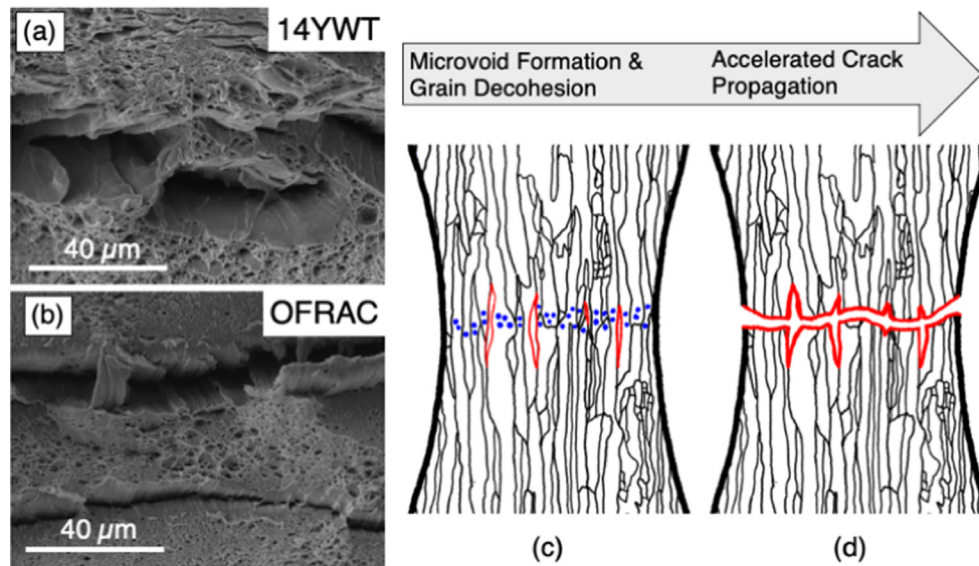aces, delamination is noted via the formation of deep crevices at some grain boundaries. This failure mechanism is described in (c) by the formation of intragranular micro-voids (blue) and grain boundary micro-cracks (red). These defects eventually lead to (d) accelerated crack propagation across the remaining load-bearing area. (For interpretation of the references to color in this figure legend, the reader is referred to the web version of this article.)

tropy associated with the elongated grain structure. Just as it has been previously demonstrated that creep [52] and fracture toughness [53] are affected by preferential grain boundary decohesion in anisotropic ODS ferritic microstructures, the tensile data reported here demonstrate orientation-specific deformability of ring tensile specimens.

Fig. 12 shows the fracture surfaces of the axial 14YWT and OFRAC specimens. The CrAZY specimen is not shown because it exhibits the same fracture characteristics as the OFRAC alloy. The surfaces of both specimens are decorated with characteristic ductile dimples, but at certain boundaries, deep crevices are observed that are attributed to sites where grain boundary decohesion occurred during the tensile test. As the Fig. 12(c-d) images illustrate, the formation of cracks in the microstructure during the tensile test could accelerate the connection of porosity and other defects along the gauge section of test specimens, thereby accelerating specimen failure. This is even more drastic in the ring-pull specimens, in which these microcracks can lead to an "unzipping" of the grain boundaries and cause catastrophic failure of the ring-pull specimen. This accelerated crack propagation via grain boundary decohesion has been previously seen in plate and rod-type geometries of ODS materials [53,54], but is underscored here since the loading direction for cladding geometries is primarily in the hoop (transverse) orientation.

One way that researchers have attempted to decrease anisotropic mechanical properties of ODS ferritic alloys is by fully recrystallizing the microstructure [4]. Owing to the remarkable thermal stability of ODS alloys, full recrystallization heat treatments create a highly stable grain structure without seriously affecting the density of nanoscale precipitates within the microstructure. Additionally, the recrystallization step usually decreases texture and improves the hoop-direction properties of thin-walled tubes [32]. In the present case, however, if the full recrystallization step for the 14YWT alloy occurs earlier in the pilgering process, the texture of this alloy is highly similar to that of the OFRAC/CrAZY alloys that remained in their cold-rolled states. Furthermore, it does not appear that the full recrystallization/grain growth heat treatment that was applied to the 14YWT alloy necessarily improved grain boundary cohesion when compared with the OFRAC alloy at room

temperature, which helps explain why limited post-yield ductility was observed for the 14YWT alloy in the ring-pull tensile results.

4. Discussion

4.1. Strengthening mechanisms for anisotropic microstructures

Significant efforts have been expended to optimize the models that researchers use to predict the macroscale behavior of nanostructured alloys. Historically, the optimization of these predictive strengthening models has been performed on alloys in early stages of thermomechanical processing (i.e. on as-extruded alloys). This type of analysis is beneficial for initial model validation, because as-extruded ODS ferritic alloys are less anisotropic and much larger quantities of material in rod or plate form have been produced over the past few decades. However, it is equally as important to be able to extrapolate the current modeling of strengthening mechanisms to components of prototypic geometry and/or microstructure. In this work, a comprehensive suite of characterization methods was applied to evaluate precipitate dispersions and dislocation densities using multiple methods. This information, coupled with the alloy and orientation-specific grain sizes/morphologies, allows for current strengthening mechanisms models to be evaluated for the thin-walled ODS tubes investigated here.

The strength of the alloys can be estimated by knowing a combination of the grain matrix hardening (σ_m), the dislocation forest hardening (σ_ρ), the strengthening by precipitates (σ_{db}), and the strengthening resulting from grain boundaries (σ_{gb}). Not only must each of these contributions be known, but it must also be determined how best to sum the individual contributions into a total combined resistance to dislocation motion. The grain boundary (Hall-Petch) hardening is estimated using:

$$\sigma_{gb} = k_{gb}/\sqrt{D_{eff}}, \tag{8}$$

where k_{gb} is the Hall-Petch coefficient for the given alloy and D_{eff} is the effective grain diameter as estimated by the method in Section 2.3.1. For the following calculations, it is assumed that the compositions of 14YWT and OFRAC are similar enough to equate

Hall-Petch coefficients and grain matrix hardening contributions. However, it is important to note that grain matrix hardening and Hall-Petch hardening were estimated for as-extruded ODS alloys with considerably less texture than the pilgered tubes analyzed in this work. Thus, each of these components must be corrected using the ratio of the orientation-dependent Taylor factor to that of an ideal BCC lattice (M/M_0, where M is the orientation-dependent Taylor factor and M_0 = 3.06). The strengthening effect of pre-existing network dislocations (forest hardening) is calculated as:

$$\sigma_\rho = M\alpha\mu b\sqrt{\rho}. \tag{9}$$

The precipitate strengthening is assumed to follow the dispersed barrier hardening model [55,56]:

$$\sigma_{db} = M\alpha\mu b\sqrt{(N_p d_p)}. \tag{10}$$

In Eqs. (9) and (10), μ is the shear modulus and b is the burgers vector for the dominant dislocation slip plane. The term ρ is the measured dislocation density, the term N_p represents the number density, and the term d_p represents the diameter of the precipitate distribution. For dislocations, it is assumed that the strengthening coefficient (α) is 0.38, whereas for precipitates, the value is a function of precipitate radius (r_p) [57]:

$$\alpha(r) = -0.017 + 0.374\log_{10}\left(\frac{r_p}{2b}\right). \tag{11}$$

It has been well established that a simple linear sum of the four constituent hardening components leads to a routine overestimation of yield stress [58]. Early efforts to reconcile this issue involved the formulation of the root-mean-square (RMS) superposition model. This model was developed under the premise that, because the resistance to dislocation glide owing to discrete obstacles is usually proportional to the square-root of the areal obstacle density, then it follows that other obstacles of similar strength should be summed in a similar manner [59]. The RMS model thus takes the form of Eq. (12):

$$\sigma_{rms,1} = \sqrt{\sigma_\rho^2 + \sigma_{db}^2 + \sigma_{gb}^2 + \sigma_m^2}. \tag{12}$$

Unfortunately, Eq. (12) usually underestimates the yield strength because the individual mechanisms vary in strength. The four strengthening mechanisms are ordered in increasing obstacle strength as: $\sigma_m < \sigma_{db} \leq \sigma_\rho < \sigma_{gb}. < \sigma_{db} \leq \sigma_\rho < \sigma_{gb}$. The precipitates and the dislocation networks have similar obstacle strengths, whereas the grain matrix hardening is a very weak obstacle that interacts over much smaller length scales. Recent studies have used a modified RMS formulation that takes into consideration the work hardening dependence of dislocation density [57]:

$$\sigma_{rms,2} = \sqrt{\sigma_\rho^2 + \left(\sigma_m + \sigma_{gb} + \sigma_{db}\right)^2}. \tag{13}$$

Equation (13) has a track record of successfully predicting yield strengths with reasonable accuracy compared to other equations/ methods. Kim et al. applied it successfully to 14YWT (SM10) over a wide range of temperatures, and they also extended it to two other ODS alloys with minimal reported error [57]. The equation was then used by other researchers in application to additional 14YWT heats with similar success [60]. Although the equation has been successful practically, it still suffers from inconsistency in how it handles obstacles with vastly different strengths such as grain matrix hardening and Hall-Petch strengthening. Consequently, one final RMS variant has received attention as a result of its application of linear summation for obstacles of highly varying strength. In Eq. (14), the weakest and strongest obstacles, grain matrix and grain boundary hardening, are added in linear summation, whereas the obstacles with intermediate strength (dislocations and precipitates) are added using the RMS approach.

$$\sigma_{rms,3} = \sigma_m + \sigma_{gb} + \sqrt{\sigma_\rho^2 + \sigma_{db}^2}. \tag{14}$$

Using the microstructural information throughout this manuscript, summarized in Table 3, strengthening calculations were compared using Eqs. (12)–(14) using four variants of precipitate and dislocation density values: $APT_{Prec.} + STEM_{Dis.}$, $EFTEM_{Prec.} + STEM_{Dis.}$, $APT_{Prec.} + XRD_{Dis.}$, $EFTEM_{Prec.} + XRD_{Dis}$. Instead of using averages to determine the individual strengthening contributions, the average and standard deviation of each measured value in this work (dislocation density, precipitate size and density, etc.) were used to generate assumed Gaussian distributions for each. Then, using a Monte Carlo approach, a random number generator would generate a value from each Gaussian distribution for subsequent input into each strengthening mechanism calculations. The same process was used to propagate potential error 10,000 times through the superposition laws to establish how differences in input variables would ultimately affect the error bars of computed yield strengths for each alloy. These estimated yield strengths were compared with the measured values from the axial tube and ring-pull specimens and are presented in Fig. 13.

The results of this comparison show that if XRD dislocation values are used, the model predicted yield strengths severely overestimate the experimentally measured strength regardless of the superposition law used. This is likely because the formation of lamellar boundaries composed of geometrically necessary dislocations is being doubly considered in both the XRD dislocation density and in the EBSD-generated grain information. The second overarching result is that, because of the higher number densities measured, APT precipitate distributions always leads to higher strengthening calculations than those using EFTEM values.

For most cases, the standard RMS Eq. (12) underestimates the strength, whereas Eqs. (13)–(14) are closer to the experimentally measured ranges. However, this simulation underscores the need for metadata comparisons between alloys of different compositions and processing histories to better optimize the hardening laws implemented for alloy design purposes. For example, if only one of these alloys was analyzed, for example 14YWT, one could conclude that Eq. (14) was most effective, but that some parametric values (such as hardening coefficients) need changing to provide better agreement between modeling and experimentation. Conversely, a different decision might be made when using evaluating the CrAZY alloy, which shows better agreement with Eq. (13). This comparison is even more valuable when considering that all three tubes investigated in this work were analyzed systematically using the same methods. This simulation exposes the need for more detailed microstructural data for anisotropic microstructures to better inform the individual models used for ODS materials design.

4.2. Precipitate coarsening vs. state-of-the-art models

It was important to ensure the tailored ODS structure survives the complex, multi-step pilgering process, or, at least, one understands and may control the precipitate coarsening – main process able to compromise the performance. In recent years, much effort has been made to model the coarsening kinetics of nanoscale precipitates in ODS FeCr and FeCrAl alloys [3,61–64]. Many of these studies have used isothermal annealing treatments on as-extruded alloys or milled powders to determine the coarsening mechanisms as well as the associated kinetics. This work provides a unique opportunity to establish the efficacy of state-of-the-art

Table 3
Alloy-specific input parameters for strengthening mechanisms calculations

Parameter	Unit	Method/Reference	14YWT-NFA1	OFRAC-OR1	CrAZY-OR1
Grain Diameter (D), Major Axis	[μm]	EBSD	74	7	13
Grain Diameter (D), Minor Axis	[μm]	EBSD	6.49	0.15	0.16
Effective Grain Diameter (D_{eff})	[μm]	EBSD	9.03	0.21	0.28
Hall Petch Coefficient (k_{gb})	[MPa/μm^2]	Cited	338 [57]		401 [40]
Taylor Factor (M) Axial	[MPa/MPa]	EBSD	2.89	3.10	3.01
Taylor Factor (M) Transverse	[MPa/MPa]	EBSD	2.88	2.72	2.66
Shear Modulus (μ)	[GPa]	Cited	81.27 [57]		
Burgers Vector (b)	[nm]	Cited	0.248 [57]		
Precipitate Diameter (d_p)	[nm]	APT	3.86 ± 1.34	3.92 ± 1.42	5.20 ± 1.58
	[nm]	EFTEM	4.66 ± 1.40	4.16 ± 1.12	5.62 ± 1.14
Strengthening Coefficient for Precipitates (α_p)	n/a	APT	0.20	0.21	0.25
	n/a	EFTEM	0.23	0.22	0.26
Precipitate Number Density (N_p)	[m^{-3}]	APT	(2.3 ± 0.8) ×10^{23}	(3.5 ± 1.2) ×10^{23}	(0.9 ± 0.2) ×10^{23}
	[m^{-3}]	EFTEM	(4.3 ± 2.1) ×10^{22}	(1.3 ± 0.2) ×10^{23}	(3.5 ± 0.7) ×10^{22}
Grain Matrix Strengthening (σ_m)	[MPa]	Cited	255 [57]		234 [40]
Strengthening Coefficient for Dislocations (α_d)	n/a	Cited	0.38 [57]		
Dislocation Density (ρ)	[m^{-2}]	STEM	(4.0 ± 1.8) ×10^{13}	(2.2 ± 1.1) ×10^{14}	(2.1 ± 1.4)×10^{14}
		XRD*	3.64 ×10^{15}	8.77 ×10^{15}	9.09 ×10^{15}

* Errors for XRD measurements are estimated to be 10% of the estimated value for error propagation analysis.
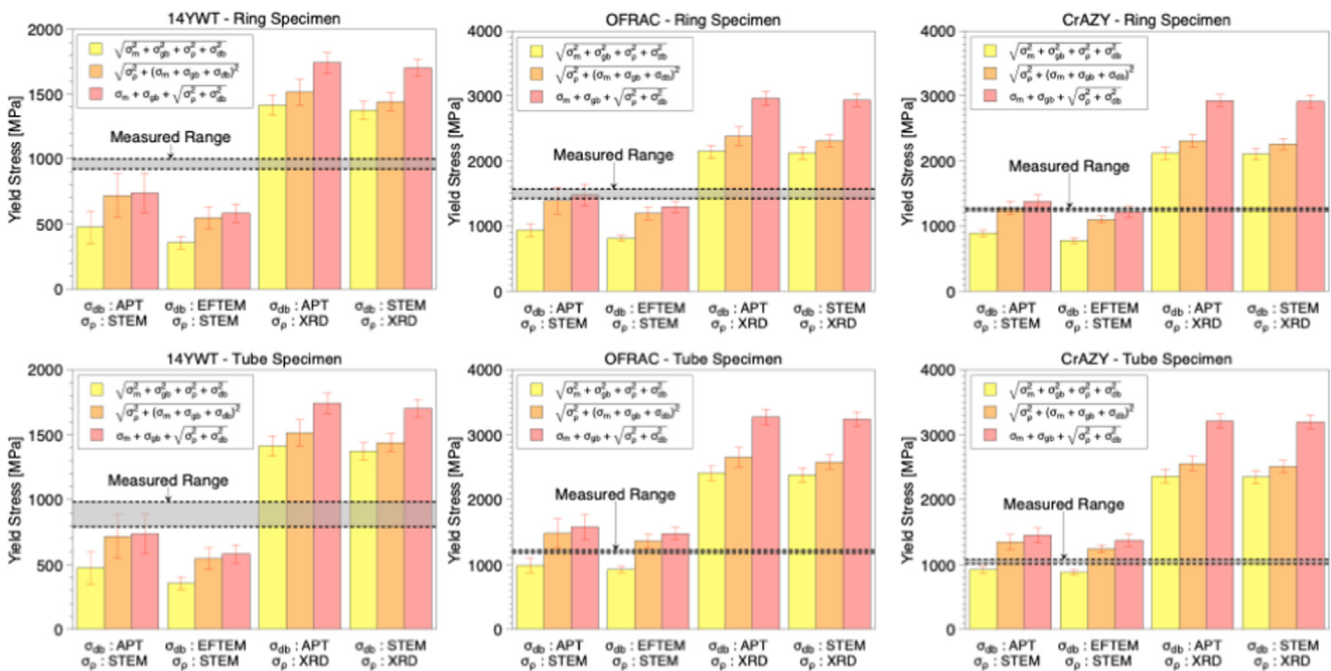

Fig. 13. Experimentally measured vs. estimated yield strengths for ring-pull and axial tube tests for 14YWT, OFRAC, and CrAZY tubes. The results are categorized as a function of the superposition approach and the method used to estimate input parameters for dislocation and precipitate characteristics. Error bars represent one standard deviation from the mean computed using a Monte Carlo error propagation approach.

models by applying them to the entire thermal histories for each of the thin-walled ODS tubes investigated here.

For ODS ferritic alloys, precipitate coarsening follows standard Ostwald Ripening theory, in which small precipitate populations dissolve at the expense of larger growing precipitates. This coarsening has been shown to be consistent with power law coarsening kinetics that can be represented by the following equation [63,65]:

$$d(T,t) = \left[k_o \exp\left(\frac{-Q}{RT}\right) t - d_0^n \right]^{\frac{1}{n}}, \quad (15)$$

where $d(T,t)$ is the time (t) and temperature (T) dependent diameter, d_0 is the original diameter of the precipitates, Q is the activation energy for the specific coarsening mechanism, R is the universal gas constant, k_o is the pre-exponential rate constant, and n is the power law exponent.

For ODS ferritic alloys, coarsening is rate limited by the 1D diffusion of solute along the network of dislocations that are pinned by the nanoscale precipitates dispersed throughout the microstructure. This dislocation pipe-diffusion mechanism corresponds to higher-order power law kinetics, usually either n = 5 or n = 6 [63–67]. Using two of the state-of-the-art coarsening models based on Eq. (15), one designed for the coarsening of (Y,Ti,O)-rich precipitates in a model ODS FeCr alloy MA957, and another designed for (Y, Al, O)-rich precipitates in ODS FeCrAl alloy CrAZY, the precipitate coarsening spanning all thermomechanical processing steps was computed and compared with the APT and EFTEM data presented in Section 3.2. Model inputs are listed in Table 4.

In the simulation, all heating and cooling rates were set to 10 °C/min as a first approximation because only the isothermal holding times are presented in Fig. 1. It has been previously

Table 4
Input parameters for precipitate coarsening estimated using Eq. (15).

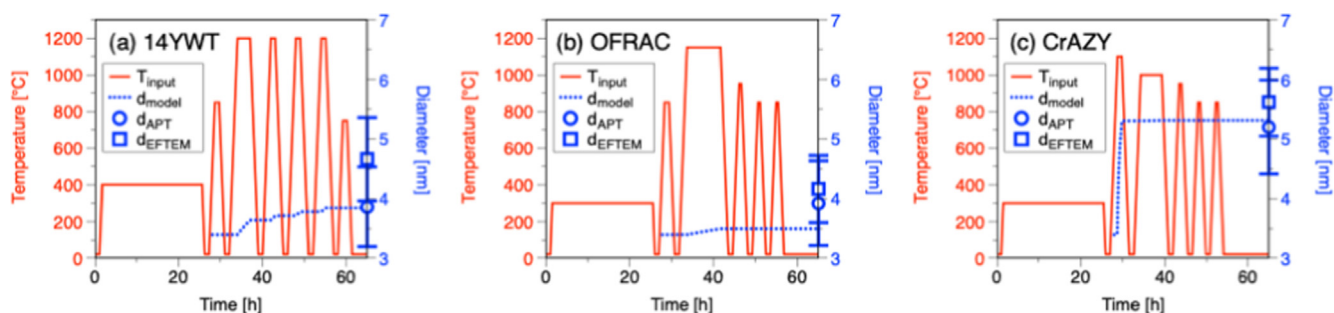| Parameter	Precipitate Type	Reference	n	$k_o [nm^n/h]$	Q [kJ/mol]
14YWT/OFRAC	(Y,Ti,O)	[63]	5	4.4×10^{25}	673
CrAZY	(Y,Al,O)	[64]	6	9.6×10^{35}	880

Fig. 14. Comparison between measured (EFTEM/APT) precipitate sizes and that estimated using state-of-the-art coarsening models. The solid red profile represents the temperature history of each tube as the original mechanically alloyed powder was subjected to degassing, extrusion, and intermediate annealing treatments during the pilgering process, and the blue line presents the model precipitate diameter at each time step. (For interpretation of the references to color in this figure legend, the reader is referred to the web version of this article.)

demonstrated that the initial distribution of nanoscale precipitates, whether (Y,Ti,O)-rich or (Y,Al,O)-rich in nature, nucleate and grow to stable sizes by 600 °C [68]. Consequently, it is assumed that at the initial heating of the extrusion step, the original precipitate distributions in each alloy are already established and that their initial diameter measures 3.4 nm, which is assumed based on the APT distributions of annealed ODS FeCrAl powder heated only to ~700 °C [64]. From this initial point, the precipitates in all three tubes could coarsen in accordance with Eq. (15) over the entire high-temperature history of the tube.

Results of the coarsening simulation are illustrated in Fig. 14. As a general rule, the models successfully predict the average precipitates size within the standard deviations reported by APT methods, although the EFTEM measurements slightly overestimate the precipitate sizes in comparison to APT. For the 14YWT alloy, the consistently high intermediate annealing temperature causes small amounts of coarsening each time. For the OFRAC alloy, most coarsening occurs during the 8 h anneal at 1150 °C before any pilgering activities. A similar trend is seen for the ODS FeCrAl CrAZY alloy, in which case the largest magnitude of coarsening occurred during the initial higher-temperature (1100 °C) extrusion step. Note that owing to the inferior coarsening resistance of the (Y,Al,O)-rich precipitates, the precipitates in the CrAZY alloy coarsened by 55% in just the 1 h anneal associated with the extrusion step.

5. Conclusions

With increasing success in designing and fabricating prototypic length-scale thin-walled tubes for advanced fission reactor applications, this international and cross-institutional collaboration has provided a strong foundation for further advances in increasing the technology readiness level for irradiation resistant ODS ferritic alloys.

The present work results describe how various thermomechanical processing differences affected dislocation densities, grain morphologies, coarsening of the precipitates, and the resulting mechanical properties. As believed, there is a need in more detailed understanding of strengthening mechanisms and adapting the existing hardening models to the post-pilgering microstructures. Nevertheless, although some anisotropy appeared between axial

and hoop properties (with accelerated grain boundary decohesion in hoop direction), the resulting microstructures, whether recovered or recrystallized, show high mechanical performance with room temperature strength exceeding 1 GPa. It was demonstrated that the ODS-structure survived the multi-step pilgering process without critical coarsening of precipitates.

CRediT authorship contribution statement

Caleb P. Massey: Investigation, Data curation, Formal analysis, Visualization, Writing – original draft. **Philip D. Edmondson:** Data curation, Resources, Writing – review & editing. **Maxim N. Gussev:** Investigation, Resources, Software. **Keyou Mao:** Investigation, Formal analysis. **Tim Gräning:** Investigation, Formal analysis, Writing – review & editing. **Thomas J. Nizolek:** Investigation, Methodology, Validation. **Stuart A. Maloy:** Conceptualization, Funding acquisition. **Denis Sornin:** Resources, Writing – review & editing. **Yann de Carlan:** Resources, Writing – review & editing. **Sebastien N. Dryepondt:** Supervision, Resources, Writing – review & editing. **David T. Hoelzer:** Supervision, Resources, Investigation, Writing – review & editing.

Declaration of Competing Interest

The authors declare that they have no known competing financial interests or personal relationships that could have appeared to influence the work reported in this paper.

Acknowledgments

Data Availability Statement

Data will be made available upon reasonable request.

References

[1] S.J. Zinkle, J.T. Busby, Structural materials for fission & fusion energy, Mater. Today 12 (11) (2009) 12–19.

[2] S.J. Zinkle, L.L. Snead, Designing radiation resistance in materials for fusion energy, Annu. Rev. Mater. Res. 44 (1) (2014) 241–267.

[3] G.R. Odette, Recent progress in developing and qualifying nanostructured ferritic alloys for advanced fission and fusion applications, Jom 66 (12) (2014) 2427–2441.

[4] S. Ukai, M. Fujiwara, Perspective of ODS alloys application in nuclear environments, J. Nucl. Mater. 307 (2002) 749–757.

[5] R.L. Klueh, J.P. Shingledecker, R.W. Swindeman, D.T. Hoelzer, Oxide dispersion-strengthened steels: a comparison of some commercial and experimental alloys, J. Nucl. Mater. 341 (2–3) (2005) 103–114.

[6] C.P. Massey, D.T. Hoelzer, P.D. Edmondson, A. Kini, B. Gault, K.A. Terrani, S.J. Zinkle, Stability of a model Fe-14Cr nanostructured ferritic alloy after long-term thermal creep, Scr. Mater. 170 (2019) 134–139.

[7] D. Gelles, Microstructural examination of commercial ferritic alloys at 200 dpa, J. Nucl. Mater. 233 (1996) 293–298.

[8] A.N. Ashong, M.Y. Na, H.C. Kim, S.H. Noh, T. Park, H.J. Chang, J.H. Kim, Influence of manganese on the microstructure and mechanical properties of oxide-dispersion-strengthened steels, Mater. Des. 182 (2019) 107997.

[9] J. Fu, J.C. Brouwer, I.M. Richardson, M.J.M. Hermans, Effect of mechanical alloying and spark plasma sintering on the microstructure and mechanical properties of ODS Eurofer, Mater. Des. 177 (2019) 107849.

[10] D.T. Hoelzer, C.P. Massey, S.J. Zinkle, D.C. Crawford, K.A. Terrani, Modern nanostructured ferritic alloys: A compelling and viable choice for sodium fast reactor fuel cladding applications, J. Nucl. Mater. 529 (2020).

[11] S.L. Dryepondt, C.P. Massey, M.N. Gussev, K.L. Linton, K.A. Terrani, M3NT-18OR020202051: tensile strength and steam oxidation resistance of ODS FeCrAl sheet and tubes, (2018).

[12] D.T. Hoelzer, Summary of Previous Mechanical Test Data on ODS Alloys 14YWT and OFRAC up to 1000°C, Oak Ridge National Lab.(ORNL), Oak Ridge, TN (United States); USDOE . . ., 2021.

[13] C.P. Massey, D.T. Hoelzer, R.L. Seibert, P.D. Edmondson, A. Kini, B. Gault, K.A. Terrani, S.J. Zinkle, Microstructural evaluation of a Fe-12Cr nanostructured ferritic alloy designed for impurity sequestration, J. Nucl. Mater. 522 (2019) 111–122.

[14] S. Dryepondt, K.A. Unocic, D.T. Hoelzer, C.P. Massey, B.A. Pint, Development of low-Cr ODS FeCrAl alloys for accident-tolerant fuel cladding, J. Nucl. Mater. 501 (2018) 59–71.

[15] L. Delannay, M.R. Barnett, Modelling the combined effect of grain size and grain shape on plastic anisotropy of metals, Int. J. Plast. 32 (2012) 70–84.

[16] G.I. Taylor, Plastic strain in metals, J. Inst. Metals 62 (1938) 307–324.

[17] M.K. Miller, K.F. Russell, Atom probe specimen preparation with a dual beam SEM/FIB miller, Ultramicroscopy 107 (9) (2007) 761–766.

[18] C.A. Schneider, W.S. Rasband, K.W. Eliceiri, NIH Image to ImageJ: 25 years of image analysis, Nat Methods 9 (7) (2012) 671–675.

[19] D.T. Hoelzer, K.A. Unocic, M.A. Sokolov, T.S. Byun, Influence of processing on the microstructure and mechanical properties of 14YWT, J. Nucl. Mater. 471 (2016) 251–265.

[20] C.M. Parish, K.G. Field, A.G. Certain, J.P. Wharry, Application of STEM characterization for investigating radiation effects in BCC Fe-based alloys, J. Mater. Res. 30 (9) (2015) 1275–1289.

[21] C.P. Massey, D.T. Hoelzer, K.A. Unocic, Y.N. Osetskiy, P.D. Edmondson, B. Gault, S.J. Zinkle, K.A. Terrani, Extensive nanoprecipitate morphology transformation in a nanostructured ferritic alloy due to extreme thermomechanical processing, Acta Mater. 200 (2020) 922–931.

[22] D. Vaumousse, A. Cerezo, P. Warren, A procedure for quantification of precipitate microstructures from three-dimensional atom probe data, Ultramicroscopy 95 (2003) 215–221.

[23] A. Cerezo, L. Davin, Aspects of the observation of clusters in the 3-dimensional atom probe, Surf. Interface Anal. 39 (2–3) (2007) 184–188.

[24] L.T. Stephenson, M.P. Moody, P.V. Liddicoat, S.P. Ringer, New techniques for the analysis of fine-scaled clustering phenomena within atom probe tomography (APT) data, Microsc. Microanal. 13 (6) (2007) 448–463.

[25] E.A. Marquis, J.M. Hyde, Applications of atom-probe tomography to the characterisation of solute behaviours, Mater. Sci. Eng.: R: Rep. 69 (4–5) (2010) 37–62.

[26] M.K. Miller, Atom Probe Tomography: Analysis at the Atomic Level, Springer Science & Business Media, 2012.

[27] M. Bachhav, G. Robert Odette, E.A. Marquis, α′ precipitation in neutron-irradiated Fe–Cr alloys, Scr. Mater. 74 (2014) 48–51.

[28] T. Ungár, A. Borbély, The effect of dislocation contrast on x-ray line broadening: a new approach to line profile analysis, Appl. Phys. Lett. 69 (21) (1996) 3173–3175.

[29] G. Williamson, W. Hall, X-ray line broadening from filed aluminium and wolfram, Acta Metall. 1 (1) (1953) 22–31.

[30] T. Ungár, I. Dragomir, Á. Révész, A. Borbély, The contrast factors of dislocations in cubic crystals: the dislocation model of strain anisotropy in practice, J. Appl. Crystallogr. 32 (5) (1999) 992–1002.

[31] D. Kriegner, Z. Matěj, R. Kužel, V. Holý, Powder diffraction in Bragg-Brentano geometry with straight linear detectors, J. Appl. Crystallogr. 48 (2) (2015) 613–618.

[32] S. Ukai, S. Kato, T. Furukawa, S. Ohtsuka, High-temperature creep deformation in FeCrAl-oxide dispersion strengthened alloy cladding, Mater. Sci. Eng., A 794 (2020).

[33] D. Sornin, U. Ehrnstén, N. Mozzani, J. Rantala, M. Walter, A. Hobt, J. Aktaa, E. Oñorbe, M. Hernandez-Mayoral, A. Ulbricht, Creep properties of 9Cr and 14Cr ODS tubes tested by inner gas pressure, Matll. Mater. Trans. A (2021) 1–12.

[34] E. Aydogan, O. El-Atwani, S. Takajo, S.C. Vogel, S.A. Maloy, High temperature microstructural stability and recrystallization mechanisms in 14YWT alloys, Acta Mater. 148 (2018) 467–481.

[35] T. Chou, H. Bhadeshia, Crystallographic texture in mechanically alloyed oxide dispersion-strengthened MA956 and MA957 steels, Metall. Trans. A 24 (4) (1993) 773–779.

[36] U.F. Kocks, C.N. Tomé, H.-R. Wenk, Texture and Anisotropy: Preferred Orientations in Polycrystals and their Effect on Materials Properties, Cambridge University Press, 1998.

[37] E. Aydogan, S. Pal, O. Anderoglu, S.A. Maloy, S.C. Vogel, G.R. Odette, J.J. Lewandowski, D.T. Hoelzer, I.E. Anderson, J.R. Rieken, Effect of tube processing methods on the texture and grain boundary characteristics of 14YWT nanostructured ferritic alloys, Mater. Sci. Eng., A 661 (2016) 222–232.

[38] B. Dubiel, W. Osuch, M. Wróbel, P. Ennis, A. Czyrska-Filemonowicz, Correlation of the microstructure and the tensile deformation of incology MA956, J. Mater. Process. Technol. 53 (1–2) (1995) 121–130.

[39] G. Pimentel, J. Chao, C. Capdevila, Recrystallization process in Fe-Cr-Al oxide dispersion-strengthened alloy: microstructural evolution and recrystallization mechanism, Jom 66 (5) (2014) 780–792.

[40] C.P. Massey, S.L. Dryepondt, P.D. Edmondson, K.A. Terrani, S.J. Zinkle, Influence of mechanical alloying and extrusion conditions on the microstructure and tensile properties of low-Cr ODS FeCrAl alloys, J. Nucl. Mater. 512 (2018) 227–238.

[41] J. Shen, H. Yang, Z. Zhao, J. McGrady, S. Kano, H. Abe, Effects of pre-deformation on microstructural evolution of 12Cr ODS steel under 1473–1673 K annealing, Nucl. Mater. Energy 16 (2018) 137–144.

[42] Y. Meng, X. Ju, X. Yang, The measurement of the dislocation density using TEM, Mater. Charact. 175 (2021).

[43] T. Malis, S. Cheng, R. Egerton, EELS log-ratio technique for specimen-thickness measurement in the TEM, J. Electron Microscopy Techn. 8 (2) (1988) 193–200.

[44] D.A. Hughes, N. Hansen, The microstructural origin of work hardening stages, Acta Mater. 148 (2018) 374–383.

[45] A.A. Kohnert, H. Tummala, R.A. Lebensohn, C.N. Tomé, L. Capolungo, On the use of transmission electron microscopy to quantify dislocation densities in bulk metals, Scr. Mater. 178 (2020) 161–165.

[46] C. Hatzoglou, B. Radiguet, P. Pareige, Experimental artefacts occurring during atom probe tomography analysis of oxide nanoparticles in metallic matrix: quantification and correction, J. Nucl. Mater. 492 (2017) 279–291.

[47] C. Hatzoglou, B. Radiguet, F. Vurpillot, P. Pareige, A chemical composition correction model for nanoclusters observed by APT - Application to ODS steel nanoparticles, J. Nucl. Mater. 505 (2018) 240–248.

[48] C.A. Williams, G.D.W. Smith, E.A. Marquis, The effect of Ti on the coarsening behavior of oxygen-rich nanoparticles in oxide-dispersion-strengthened steels after annealing at 1200°C, Scr. Mater. 67 (1) (2012) 108–111.

[49] C.A. Williams, P. Unifantowicz, N. Baluc, G.D.W. Smith, E.A. Marquis, The formation and evolution of oxide particles in oxide-dispersion-strengthened ferritic steels during processing, Acta Mater. 61 (6) (2013) 2219–2235.

[50] C.P. Massey, P.D. Edmondson, K.A. Unocic, Y. Yang, S.N. Dryepondt, A. Kini, B. Gault, K.A. Terrani, S.J. Zinkle, The effect of Zr on precipitation in oxide dispersion strengthened FeCrAl alloys, J. Nucl. Mater. 533 (2020).

[51] B. Hary, R. Logé, J. Ribis, M. Mathon, M. Van Der Meer, T. Baudin, Y. de Carlan, Strain-induced dissolution of Y-Ti–O nano-oxides in a consolidated ferritic oxide dispersion strengthened (ODS) steel, Materialia 4 (2018) 444–448.

[52] T. Jaumier, S. Vincent, L. Vincent, R. Desmorat, Creep and damage anisotropies of 9%Cr and 14%Cr ODS steel cladding, J. Nucl. Mater. 518 (2019) 274–286.

[53] M.J. Alinger, G.R. Odette, G.E. Lucas, Tensile and fracture toughness properties of MA957: implications to the development of nanocomposited ferritic alloys, J. Nucl. Mater. 307–311 (2002) 484–489.

[54] M.E. Alam, S. Pal, K. Fields, S.A. Maloy, D.T. Hoelzer, G.R. Odette, Tensile deformation and fracture properties of a 14YWT nanostructured ferritic alloy, Mater. Sci. Eng., A 675 (2016) 437–448.

[55] A.K. Seeger, in: Proceedings of the second United Nations International Conference on the Peaceful Uses of Atomic Energy, vol. 6, United Nations, New York, 1958, p. 250.

[56] S.J. Zinkle, Y. Matsukawa, Observation and analysis of defect cluster production and interactions with dislocations, J. Nucl. Mater. 329–333 (2004) 88–96.

[57] J.H. Kim, T.S. Byun, D.T. Hoelzer, C.H. Park, J.T. Yeom, J.K. Hong, Temperature dependence of strengthening mechanisms in the nanostructured ferritic alloy 14YWT: Part II—Mechanistic models and predictions, Mater. Sci. Eng., A 559 (2013) 111–118.

[58] G.R. Odette, G.E. Lucas, Recent progress in understanding reactor pressure vessel steel embrittlement, Radiat Eff. Defects Solids 144 (1–4) (2006) 189–231.

[59] P. Haasen, V. Gerold, G. Kostorz (Eds.), Strength of Metals and Alloys, Vol. 3, Pergamon Press, Oxford, 1979.

[60] E. Aydogan, S.A. Maloy, O. Anderoglu, C. Sun, J.G. Gigax, L. Shao, F.A. Garner, I.E. Anderson, J.J. Lewandowski, Effect of tube processing methods on microstructure, mechanical properties and irradiation response of 14YWT nanostructured ferritic alloys, Acta Mater. 134 (2017) 116–127.

[61] L. Barnard, N. Cunningham, G.R. Odette, I. Szlufarska, D. Morgan, Thermodynamic and kinetic modeling of oxide precipitation in nanostructured ferritic alloys, Acta Mater. 91 (2015) 340–354.

[62] X. Boulnat, M. Perez, D. Fabrègue, S. Cazottes, Y. de Carlan, Characterization and modeling of oxides precipitation in ferritic steels during fast non-isothermal consolidation, Acta Mater. 107 (2016) 390–403.

[63] N.J. Cunningham, M.J. Alinger, D. Klingensmith, Y. Wu, G.R. Odette, On nano-oxide coarsening kinetics in the nanostructured ferritic alloy MA957: a mechanism based predictive model, Mater. Sci. Eng., A 655 (2016) 355–362.

[64] C.P. Massey, S.N. Dryepondt, P.D. Edmondson, M.G. Frith, K.C. Littrell, A. Kini, B. Gault, K.A. Terrani, S.J. Zinkle, Multiscale investigations of nanoprecipitate nucleation, growth, and coarsening in annealed low-Cr oxide dispersion strengthened FeCrAl powder, Acta Mater. 166 (2019) 1–17.

[65] G.R. Odette, On the status and prospects for nanostructured ferritic alloys for nuclear fission and fusion application with emphasis on the underlying science, Scr. Mater. 143 (2018) 142–148.

[66] N. Oono, K. Nakamura, S. Ukai, T. Kaito, T. Torimaru, A. Kimura, S. Hayashi, Oxide particle coarsening at temperature over 1473 K in 9CrODS steel, Nucl. Mater. Energy 9 (2016) 342–345.

[67] N.H. Oono, S. Ukai, S. Hayashi, S. Ohtsuka, T. Kaito, A. Kimura, T. Torimaru, K. Sakamoto, Growth of oxide particles in FeCrAl- oxide dispersion strengthened steels at high temperature, J. Nucl. Mater. 493 (2017) 180–188.

[68] A. Deschamps, F. De Geuser, J. Malaplate, D. Sornin, When do oxide precipitates form during consolidation of oxide dispersion strengthened steels?, J Nucl. Mater. 482 (2016) 83–87.